ORIGINAL ARTICLE

A comparative insight into the mechanical properties, antibacterial potential, and cytotoxicity profile of nano-hydroxyapatite and nano-whitlockite-incorporated poly-L-lactic acid for bone tissue engineering

Farzana Nazir[1] · Laraib Abbas[1] · Mudassir Iqbal[1] ⓘ

Abstract

This work reports the synthesis and characterization of nanohydroxyapatite (nHA) and nanowhitlockite (nWH), which were further incorporated to poly-L-lactic acid (PLLA) to study their effects on the structure, mechanical properties, antibacterial potential, and cytotoxicity of PLLA. SEM images of PLLA–nHA and PLLA–nWH revealed uniform dispersion of nanoparticles in polymer. FTIR spectroscopy showed shift in functional group position and indicated transformation of PLLA α′ to more crystalline PLLA α, which was further confirmed by X-ray diffraction. The mechanical properties of the materials showed that addition of nanoparticles have made PLLA ductile and strong pertaining to the effective dissipation of loads across the interfaces, enabling them to delay the crack growth by avoiding stress concentration sites. PLLA–nWH10% showed the highest antibacterial activity against Gram-positive bacteria *Listeria monocytogenes* and *Staphylococcus aureus*. In vitro cytocompatibility of PLLA–nWH10% was highest, 98%, at day 7 against fibroblasts MC3T3-E1 (osteoblastic cell line), whereas all nanocomposites have enhanced cell viability (94%) as compared to pure PLLA. Alizarin red assay showed twofold increase in calcification at day 14 with PLLA–nWH as compared to PLLA–nHA. It was clearly observed that binary system PLLA–nWH at all concentrations had good dispersion and interfacial interaction resulting in improved mechanical and enhanced osteoconductive properties as compared to PLLA–nHA.

Keywords Poly-L-lactide · Hydroxyapatite · Whitlockite · Mechanical properties · Bone tissue engineering

Introduction

Biomaterials containing calcium phosphate moieties, such as hydroxyapatite (HAP: $Ca_{10}(PO_4)_6(OH)_2$), dicalcium phosphate dehydrate (brushite), tetracalcium phosphate, and tricalcium phosphate (TCP) have been reported to induce osteogenesis in stem cells leading to bone tissue formation and are known to be a suitable bone filler for bone defects (Farokhi et al. 2018; Nazeer et al. 2017; Nie et al. 2017; Nosrati et al. 2020a). Bone, a heterogeneous material, is made up of mineral phase analogous to HA and an organic phase which constitute 70% and 30% of the bone, respectively.

Collagen type 1 comprises 90% of the organic matrix and the other 10% is composed of proteoglycans and non-collagenous proteins. Microscopically, bone is composed of three types of cells, osteoblasts, osteocytes and osteoclasts, where osteoblast and osteocyte are bone-forming cells, while osteoclasts resorb bone cells. Bone formation is a sophisticated marvel which depends on the participation of the inorganic mineral deposition at the bone generation and remodeling (Harb 2020; Hu et al. 2020; Mohseni et al. 2018). However, this process still needs full elucidation and illustration. Looking closely into the bone regeneration site, recent reports suggest that another phase is also involved in the bone remodeling. Because osteoclastic activity was observed for a bone mineral whose structure is very close to HAP and subsists in acidic pH, which is contrary to the well-maintained fact that HAP is not stable at acidic pH usually found at the site of bone regeneration. Recent insight into this problem reveals that the inorganic phase

✉ Mudassir Iqbal
mudassir.iqbal@sns.nust.edu.pk

1 Department of Chemistry, School of Natural Sciences (SNS), National University of Science and Technology (NUST), Islamabad 44000, Pakistan

or mineral involved in bone is none other than whitlockite (WH: $Ca_{18}Mg_2(HPO_4)_2(PO_4)_{12}$). Interestingly, 99% of calcium (Ca^{2+}) is found in mineralized bone in the form of HA, while 50% magnesium (Mg^{2+}) is stored in bones and exists in WH (Teitelbaum 2000; Silver et al. 1988; Wu et al. 2020).

WH is found to be the second most abundant inorganic phase in bones, approximately 20% based on the amount of (Mg^{2+}), while it is abundantly found in the human dentin consisting of 56% of the calcified part of the bone (Jang et al. 2016). WH exists in addition to hydroxyapatite, and the ratio of WH is higher in younger persons and during early bone mineralization. Interestingly, WH has close resemblance to its synthetic equivalent *b*-tricalcium phosphate (b-$Ca_3(PO_4)_2$), but has stable regions in phase and has HPO_4^-. WH is found in short range in hard tissues with elevated dynamic loading and is stable at acidic pH as compared to HA (Muthiah Pillai et al. 2019). Magnesium (Mg^{2+}), and phosphate (PO_4^{3-}) of synthetic nanoWH (nWH) have been reported to induce bone regeneration and inhibition of osteoclastic differentiation (Kim et al. 2017).

Difficulty in detection and precipitation methods were the major hindrances to explore the role of WH in bone remodeling. This has been resolved by the pure precipitation method reported by Jang et al. (2015). The chemical precipitation method involves the synthesis of nanoWH (nWH) by using ternary aqueous system in acidic condition with limited Mg^{2+} ions (Jang et al. 2014). However, HA was synthesized via hydrothermal and solvothermal method with and without argon gas injection to investigate the effect of different synthesis techniques on its mechanical properties (Nosrati et al. 2020a, b, c, d).

A comparative study of nWH, nHA and TCP revealed the superior properties of nWH for in vitro differentiation as compared to nHA. nWH in another study has proven to be a "living bone mineral", a smart biomaterial to induce self-healing of bone (Kim et al. 2017; Jin et al. 2019). Synergistic studies of nHA and nWH for mesenchymal stem cell differentiation revealed that both minerals need optimal values for bone regeneration (Cheng et al. 2018). WH has antibacterial properties (Chandran et al. 2020), has been employed as an injectable material for hemostasis (Muthiah Pillai et al. 2019), and has enhanced bone regeneration as compared to HA and TCP in rabbit ilium defect (Jin et al. 2019).

For the development of high-performance and multifaceted materials, modifying existing material is one of the trending approaches in the field of science and technology. Various chemical and physical methods have been applied for modification such as composites and nanocomposites and copolymerization. Polymeric fourth- generation nanocomposites are used for bone tissue engineering (Nazir et al. 2021a). PLLA is a polyester, biopolymer, approved by the Food and Drug Authority (FDA), and is widely used for bone tissue engineering (Oustadi et al. 2020; Christy

2020; Raghavendran 2021). PLLA has hydrophobicity and weak mechanical properties which are often resolved by adding HA in PLLA (Doosti-Telgerd et al. 2020; Mondal et al. 2020; Kaya et al. 2019; Pavia et al. 2018; Yang et al. 2018). The Strategy of using organic polymer (PLLA) and inorganic nanofiller (HA) has synergistic effects of the continents and it also mimics the native bone structure (Kanani and Bahrami 2010; Rodenas-Rochina et al. 2015). WH is a relatively new material revisited for bone tissue engineering. The nWH scaffold with PLLA can be a potential contender for future bone tissue engineering scaffolds. To the best of our knowledge, no reports of PLLA/nWH are found in literature.

Herein, we report laboratory-synthesized nHA and nWH and then we demonstrated the effect of different nanoparticle concentrations on the PLLA. Further, we explored and compared how these two bone ceramics can recapitulate early stage of bone regeneration by checking their mechanical properties, degradation rate and cytotoxicity studies. Our hypothesis was to check the improved bone regeneration by continuous supply of PO_4^{3-} and Mg^{2+} from nWH under physiological conditions. In vitro studies revealed that enhanced cell attachment and proliferation were witnessed in the case of PLLA–nWH.
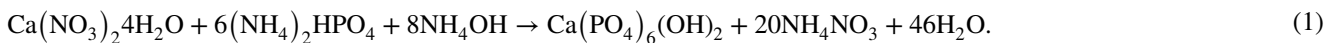
Experimental section

Materials and reagents

PLLA, M_n 40,000 (M_n = number average molecular mass), and chloroform research grade (99% pure) were acquired from Merck (USA). Calcium hydroxide ($Ca(OH)_2$) (ACS reagent, ≥ 95.0%), magnesium hydroxide ($Mg(OH)_2$) (reagent grade, 95%), ammonia solution (35%), and certified AR for analysis, d = 0.88, were purchased from Fisher Chemicals. Calcium nitrate tetrahydrate ($Ca(NO_3)_2 \cdot 4H_2O$), diammonium hydrogen phosphate ($(NH_4)_2HPO_4$), and phosphoric acid (H_3PO_4) (ACS reagent, ≥ 85 wt% in H_2O%) were purchased from Sigma-Aldrich Co., USA. Calcium nitrate tetrahydrate ($Ca(NO_3)_2 \cdot 4H_2O$) reagent grade, ACS molecular weight 236.15 g mol^{-1} assay (complexometric assay 99–103%), diammonium hydrogen phosphate ($(NH_4)_2HPO_4$), reagent grade, ACS molecular weight 132.06 g mol^{-1} (98%), and deionized water were acquired from Dae-Jung, (Korea) and used as such.

Synthesis of the hydroxyapatite nanoparticles

Hydroxyapatite nanoparticles (nHA) synthesis was carried out by combining calcium ($Ca(NO_3)_2 \cdot 4H_2O$) and phosphorus ($(NH_4)_2HPO_4$) sources by maintaining pH 12 using NH_3 sol (Amin et al. 2015). Briefly, aqueous solutions of Ca

$(NO_3)_2\cdot4H_2O$ (dissolving 32.8 g in 200 ml deionized water at 80 °C) and $(NH_4)_2HPO_4$ (9.5 g in 137.5 ml in deionized water at 80 °C) were prepared on a magnetic hot plate. Afterward, dropwise addition of $Ca(NO_3)_2\bullet4H_2O$ solution into highly basic $(NH_4)_2HPO_4$) solution for 2 h at 80 °C was followed by 24 h of aging. After aging, nHA precipitates were filtered and washed with deionized water. Residual nHA was vacuum oven dried at 80 °C for 24 h. Muffle furnace was used for calcination at 500 °C for 2 h. The chemical reaction for the synthesis of nHA is described in Eq. (1):

considering Bragg's peaks (211) and (310) $D = k\lambda/\beta \cos(\theta)$, where D represents crystal size, k = shape factor (0.008), λ = incident wavelength, β = broadening of peak at half of the maximum peak, and θ is diffraction angle. XRD of PLLA–nHA, and PLLA/nWH was carried out by keeping a step size of 0.04. Nanocomposites were scanned over a range of 2θ 5°–70°. Bruker Vertex 70 FTIR-ATR spectrophotometer was used to record vibrational band spectra at wavenumber 550–4000 cm^{-1}. Dried thin films of the PLLA–nHA, and PLLA/nWH were placed to get IR data.

$$Ca(NO_3)_2 4H_2O + 6(NH_4)_2HPO_4 + 8NH_4OH \rightarrow Ca(PO_4)_6(OH)_2 + 20NH_4NO_3 + 46H_2O. \qquad (1)$$

Synthesis of the whitlockite nanoparticles

Whitlockite is synthesized by previously reported wet chemical precipitation method (Kim et al. 2017; Jang et al. 2015; Jang et al. 2014), in which $Ca(OH)_2$ and $Mg(OH)_2$ were taken as preliminary reagents. Initially, 0.37 M of $Ca(OH)_2$ and 0.13 M $Mg(OH)_2$ solutions were prepared in distilled water. Then, equal proportions of $Ca(OH)_2$ and $Mg(OH)_2$ were mixed in distilled water by keeping the temperature of the system below that of boiling water. A suitable quantity of 0.5 M H_3PO_4 was added in a dropwise manner into the $Ca(OH)_2$–$Mg(OH)_2$ solution at the speed of 12.5 ml min^{-1} along with continuous stirring. The resulting precipitates were aged for 24 h to obtain particles of sufficient size and then assembled using a filter press. The nanocomposites were calcined at appropriate temperature for a sufficient time to remove any volatile impurities.

Synthesis of PLLA/nHA and PLLA/nWH nanocomposites

Solvent casting method was used to prepare PLLA nanocomposites. PLLA–nHA or PLLA–nWH composites with different concentrations (100–0%, 99–1%, 95–5%, and 90–10% w/w, respectively) were prepared by accurately weighing in a reagent bottle and homogenously dissolved in 30 ml of chloroform using a magnetic stirrer at room temperature for 2 h. Later, this homogenous viscous solution was air dried in a Petri dish at room temperature for 24 h. Nanocomposite films were further dried in a vacuum oven at 50 °C for 12 h to remove any traces of solvent left behind. Dried nanocomposite films were stored at room temperature till further use.

Characterization techniques

To confirm the crystal structure and homogeneity of HA and WH powder, XRD was performed (model: DRON8, country: Russia), with voltage 40 kV and current 20 mA. The average crystallite size was calculated by using Scherer's formula

Morphological analysis of the nanocomposite films was acquired by using JSM-6490LV by JEOL Nanoparticle morphology and the size was observed by placing powder nanocomposites on carbon tape and then gold sputtering the powdered nanoparticles. Nanoparticles were also suspended in deionized water, and then after water evaporationthe nanocomposites were gold sputter coated for SEM analysis. Cryo-fractured morphology of pure polymer films, blend films and nanocomposite films was determined. Nanocomposite films were dipped in liquid nitrogen and then broken to produce fresh cryo-fractured surface. These nanocomposite surfaces were attached to aluminum stub, followed by gold sputtering of these nanocomposite films for their examination by SEM. Nanocomposites were photographed at various magnifications. Taking images at higher magnification was unlikely, because of the breakage of the polymer strips at magnification more than 10,000×.

Trapezium-X Universal Testing Machine (AG-20KNXD Plus) built by Shimadzu Corporation was tapped to investigate the tensile mechanical properties whose crosshead speed was set at 1 mm min^{-1}. The nanocomposite films for these analysis tests were prepared by slicing films with a gauge length of 20 mm in dimensions of 10 mm × 50 mm (width × length) by using a hand cutter (ASTM D6287).

Antibacterial test: Disc diffusion assay to evaluate the antibacterial potential of PLLA–nHA, and PLLA/nWH was carried out against bacteria. Bacterial culture of two Gram-positive strains, namely *Listeria monocytogenes* and *Staphylococcus aureus,* and one Gram-negative strain, *Escherichia coli*, was freshly prepared in nutrient broth to the logarithmic phase at 37 °C in an orbital shaker for 16–18 h. Solutions with optical density between 0.58 and 0.6 at 600 nm were diluted to 10^6–10^5 CFU ml^{-1}. Nanocomposite films of equal size of 8 mm diameter were disinfected with 70% ethanol for 1 h and then under UV for 15 min. Sterile Petri dishes were inoculated with 100 µl of each equalized bacterial nanocomposite to create a uniform lawn on each Petri plate. Nanocomposite discs were placed on the bacterial lawn at equal distance. Antibacterial pallet of Gemifloxacin was used as a

positive control and pure polymer as negative control were used. Nanocomposite films were incubated for 16 h at 37 °C. Each nanocomposite was tested in triplicate.

To carry out the swelling test of nanocomposite films, films of dimensions 10 mm × 10 mm were weighed down and then sealed by placing in already weighed Eppendorf tubes containing 1 ml of PBS, followed by placement of Eppendorf in a shaker at a temperature of 37 °C. Upsurge in the weight can be credited to the water absorption, was measured by removing nanocomposite films from PBS at specific time periods, and blotting them with an absorbent tissue. A fresh aliquot of PBS was added to the Eppendorf daily. To obtain reproducibility in results, four nanocomposite films were examined for each time interval till equilibrium was attained. The remaining weight percentage (wt%) was calculated.

In vitro degradation test was carried out by measuring weight loss in collagenase type II solution prepared in PBS and incubating them at 37 °C. While nanocomposite film dimensions were of 10 mm × 10 mm size. To determine the remaining weight percent, triplicate nanocomposite films were freeze dried overnight before taking weight measurements at specific time periods.

Cell viability tests

To assess the biocompatibility of the PLLA blends, cell culture fibroblast cell lines NIH3T3 and mouse precursor osteoblast cell lines MC3T3-E1 were taken. Frozen cell lines were passed through DMEM five times, along with 1% Penstrep and 10% FBS and then incubated at 37 °C temperature, followed by incubating through humidified air containing 5% CO_2. The culture media was changed every other day and after confluence of 70% cells passed through. First, all nanocomposite films were cut into circular shaped discs having diameter of 15 mm. After that, these nanocomposite films were disinfected for 2 h with 70% ethanol, followed by washing with PBS prior to in vitro cell analysis. Test nanocomposite films were inhabited in a 24-well sterilized tissue culture plate and compressed. Seeding of the fibroblast cell lines NIH3T3 and osteoblastic cell line MC3T3-E1 onto the nanocomposite discs was done at a strength of 1×10^4 cells well^{-1}. Then, cells were cultured for 1, 3, and 7 days in whole DMEM media containing 1% Penstrep and 10% FBS. Cell culture media were subsequently removed after 1, 3 and 7 days, respectively. Cell viability reagent, that is, 10% PrestoBlue grown in DMEM was reared in cells for 120 min at 37 °C, followed by transfer of 100 μl of reared cell viability reagent onto 96-well plate. To calculate the cell viability, reading of the plate was performed on a plate

reader whose fluorescence intensity of excitation and emission was found to be 535–560 nm and 590–615 nm, respectively. For this cell culture analysis, triplicate nanocomposite films were examined in three independent experiments. All resulting data were presented at an average ± standard deviation and the numerical value of significant difference was taken as $p < 0.05$. To make a comparison of all pairs of columns test for statistical comparison, one-way ANOVA test was carried out by applying Tukey's method. In figures, $*p \le 0.05$, $**p \le 0.01$, $***p \le 0.001$ are designated as statistical significance.

LIVE/DEAD assay Viability/Cytotoxicity Kit (mammalian cells) was utilized to conduct NIH-3T3 and MC3T3-E1 at 1, 3, and 7 days. The protocol was followed for cell culturing. Control was set with untreated cells. PBS and calcein AM (1 μl ml^{-1} of 50 μm stock) were used to wash cells and then 50 μl ethidium homodimer-1 (2 μl ml^{-1} of the 2 mm stock) was added to each well. After incubation for 30–40 min, cells attached to nanocomposite films were viewed with inverted fluorescence microscope (Zeiss Axio Observer Z1, Zeiss, USA). For calcein AM, cells attached to the nanocomposite films were incubated for 30–40 min and then observed on inverted fluorescence microscope. The wavelength of 494/517 nm was set for calcein AM (green shows live cells indicating intracellular esterate activity) and 528/617 nm. Cell count of live cells was done with Image J software of four random fields of three replicates of nanocomposite films. 10× random field images were taken. The total number of live cells was divided by the total number of cells to calculate the percentage of live cells.

F-actin/DAPI staining was done to examine cell proliferation and adhesion after 1, 3 and 7 days of NIH3T3 and MC3T3-E1on nanocomposite films. Cell staining was done by first removing the media, then rinsed with PBS and fixed using 4% PFA for 15 min. 0.1%Triton X-100 solution was introduced for 30 min for permeabilization. After that, 1% BSA for an hour was added. F-actin/DAPI mixed in PBS was fixed in the wells. Inverted fluorescence microscope was used to visualize cells and from triplicate nanocomposite films, their random images were captured (Zeiss Axio Observer Z1, Zeiss, USA).

Mineralization (calcium deposition) was checked by performing Alizarin Red assay. MC3T3-E1 (mouse precursor osteoblast cell lines) and nanocomposites films were seeded 1×10^3 cells well^{-1} and cultured (37 °C and 5% CO_2) for 14 days. On day 14, media were removed and washed with PBS and cells were fixed with 4% PFA for 15 min after removing media. 1% Alizarin red in PBS was used to stain nanocomposite films for 45 min, and after rinsing with PBS it was visualized under fluorescence microscope (Zeiss Axio Observer Z1, Zeiss, USA).

Results and discussion

Wide angle XRD of the nanoparticles and nanocomposite films

XRD was carried out for the phase confirmation of the synthesized nanoparticles. XRD pattern shown in Fig. 1b has characteristic appearance of Bragg's reflections of nHA at 2θ 25.8°, 31.9°, 32.9°, 34.0° and 39.8°, corresponding to the crystal planes of HA (002), (211), (300), (202) and (310), respectively, matches the JCPDS/ICDD No. 09-0432, and is in accordance with the already reported data (Nosrati et al. 2020a, c, d; Klinkaewnarong and Utara 2018). The crystallite size of synthesized nanoparticles by using Scherer formula was found to be 22.3 nm. Phase confirmation of the synthesized nWH was matched with the JCPDS /ICDD No. 70-2064 and confirmed homogenous phase as already reported in literature (Muthiah Pillai et al. 2019). Diffraction peaks of nWH were observed (Fig. 1a) at 2θ 17.1° 25.96°, 28.02°, 31.32°, 32.9°, and 34.56°, 37.72°, 44.16°,

corresponding to the crystal planes of HA (110), (101), (214), (300), (0210) and (220), (Jang et al. 2014, 2016; Kim et al. 2017; Cheng et al. 2018) The crystallite size of nanoparticles having rhombohedral crystal structure was found to be 19.11 nm.

X-ray diffraction pattern of PLLA shows pattern 14.93°, 16.76°, 18.96°, 25.4°. PLLA had pseudohexagonal crystalline structure, which can be accredited to looser chain packaging and marginally larger unit cell dimension indicated by the broad peaks and at lower angles 16.4° and 18.7° (Fig. 1c). On addition of the nanoparticles WH and HA, we clearly observed that the intensity of the peaks increased and there was a shift in the peak positions. For PLLA–nWH, PLLA peaks were observed at planes (110)/(200) at angle 16.7°, and (203)/(113) at angle 19.0° and other planes (011) and (211) reflected at angle 14.6° and 22.3°. WH incorporation PLLA–nWH was indicated by the appearance of the peaks at 26.45° (101) and 29.23° (214) where the intensity of the peak increased upon increasing the concentration of the nWH (Fig. 1c). Similarly, for PLLA–nHA integral
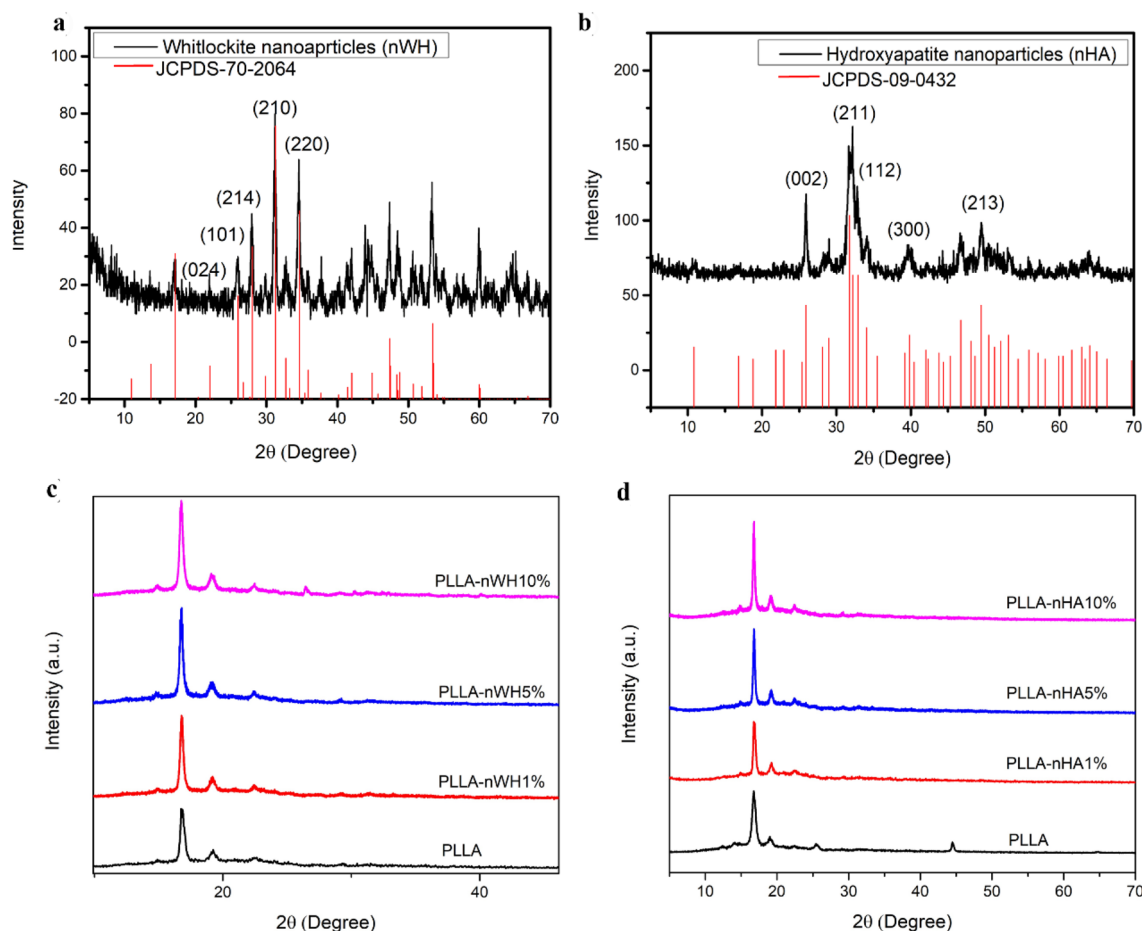

Fig. 1 XRD of **a** nWH, **b** nHA, **c** PLLA/nWH, and **d** PLLA/nHA. Integral values of peak intensity increased with addition of nanoparticles

intensity of the nHA peaks at 25.8° and 34.0°, corresponding to the (002) and (211) reflections, increased on increasing nHA concentrations (Fig. 1d). In nanocomposite, the shifting of the characteristic peak position reflects the impact of nanophase on the crystal structure of the PLLA. On addition of nHA into the polymer matrix, it was observed that the diffraction peaks appeared at values assigned in the literature to the α forms of PLLA (parameters of the PLLA unit cell are: $a = 1.06$ nm, $b = 0.106$ nm and $c = 2.88$ nm) (Beltrán et al. 2016). In nanocomposites, diffraction peaks of PLLA became sharp and stronger as compared to the neat PLLA, which confirms the nucleation effect of nHA or nWH on PLLA chains. This phenomenon was supported by the reported work of MC (Righetti et al. 2017, 2018) and IGI (Athanasoulia et al. 2017). At different concentrations 1–10% of nHA and nWH, increasing intensity of the peak was indicated, showing that the nanoparticle was acting as a nucleating agent for PLLA, causing increased orientation, alignment, and closer packing of the PLLA chains, resulting in increases in the crystallinity of PLLA. Further crystal structure was evaluated by FTIR.

FTIR analysis of the nanoparticles and nanocomposite films

FTIR was carried out to check the interaction between the inorganic filler and organic polymer matrix in nanocomposites. No chemical degradation of any constituent materials was indicated in the FTIR spectra. The synthesized nHA compound was subjected to FTIR as shown in Fig. 2b. The presence of peaks at 1092 (PO_4^{3-}, ν_1), 1023 (PO_4^{3-}, ν_1), 963 (OH^{-1}), 601 (HPO_4^{2-}), and 561 cm^{-1} (PO_4^{3-}, ν_3) were the characteristic bands for nHA, as corroborated in the literature (Nosrati et al. 2020b; Gieroba 2021). A very small
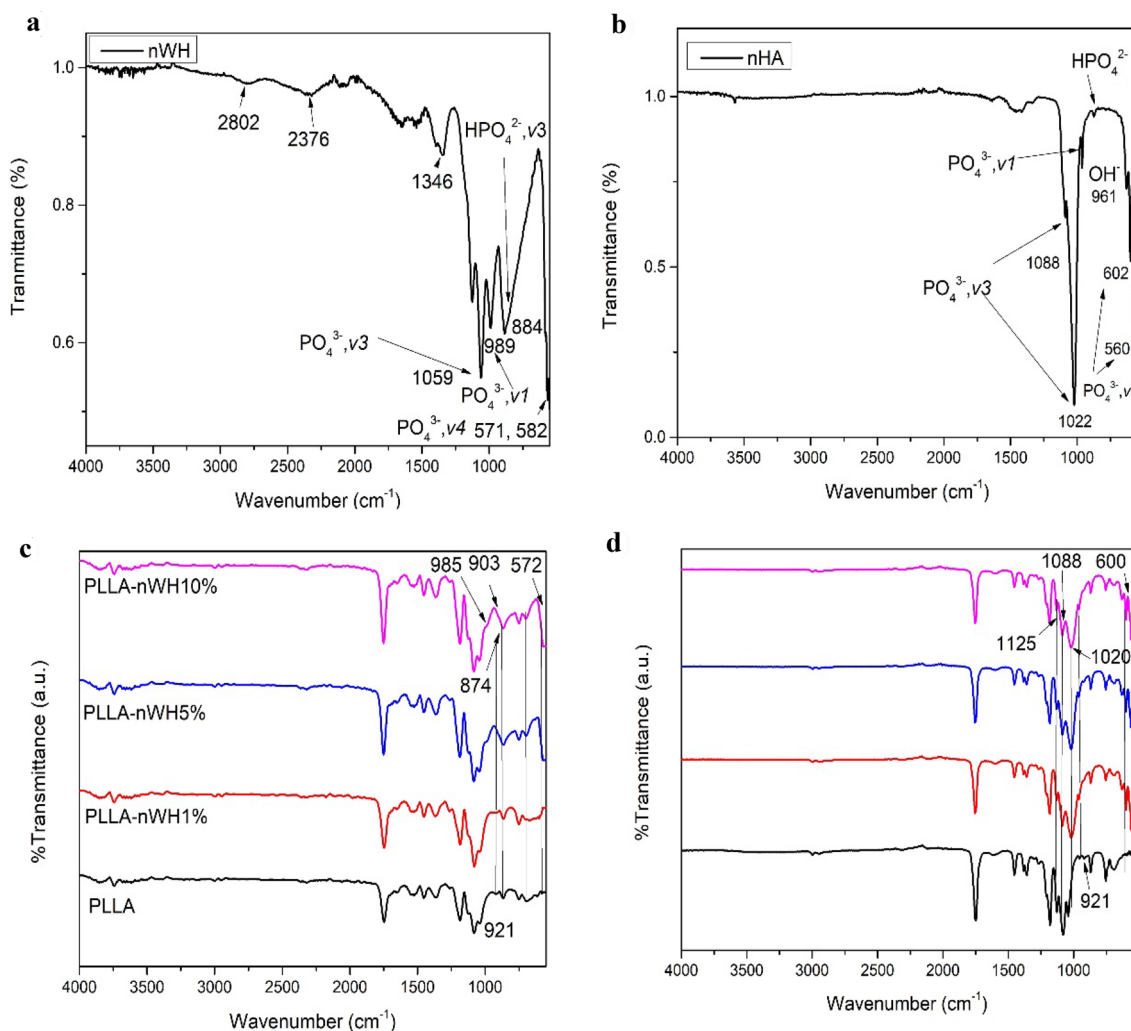
Fig. 2 FTIR of **a** nHA, **b** nWH, **c** PLLA/nWH, and **d** PLLA/nHA. Addition of nanoparticle affected the IR spectra below 2000 cm^{-1}. Physical interaction of hydrogen bonding was found below 1000 cm^{-1}

peak of OH was visible at 3571 cm^{-1}. The amount of H$_2$O was very low. Particularly, the band at 963 cm^{-1} was a distinguishable peak observed for asymmetric P–O stretching vibration of PO$_4^{3-}$ (Sroka-Bartnicka et al. 2017). In addition, a medium sharp peak appeared at 631 cm^{-1} corresponding to the O–H deformation mode. FTIR bands for nWH are shown in Fig. 2a. The characteristic vibrational bands of nWH were observed at 571 cm^{-1} and 582 cm^{-1} double peak (ν4, bending of PO$_4^{3-}$), 989 cm^{-1} (ν1, P–O–H stretching of HPO$_4^{2-}$), 884 cm^{-1} (ν3, HPO$_4^{2-}$ bending), and 1059 cm^{-1} (ν3 of PO$_4^{3-}$) bending (Kaliannagounder 2021; Capitelli et al. 2021; Wang et al. 2020). Relatively sharp peak at 1346 was assigned to P(O–H) (Cooper et al. 2013), while two bands at 2374 and 2794 cm^{-1} were assigned to P–O overtone on the basis of previous reports (Capitelli et al. 2021).

Figure 2c. d displays the FTIR spectra of the nanocomposites upon incorporation of nWH and nHA in PLLA. PLLA characteristic peaks 1755, 1187, and 1082 cm^{-1} related to C=O stretch, CH$_3$ stretch and COC were observed. CH$_3$ stretch weak bands were present at 2946 and 2996 cm^{-1} (Oner et al. 2021). A characteristic band at 1755 cm^{-1} showed splitting and thus suggesting the amorphous nature of the PLLA or this can be attributed to the presence of α' crystal structure. In case of nanocomposites, clearly, we observed the changes in the three regions of spectra: one was the carbonyl (C=O) stretching area 1800–1700 cm^{-1}, second was the CH$_3$ and CH bending region in the area 1500–1300 cm^{-1}, while the third was the COC stretching area between 1300 and 950 cm^{-1}. There was no evidence of chemical bonding between nanoparticles and PLLA. On addition of both, the nanoparticles band intensity at 1758 cm^{-1} increased and became sharp, showing no splitting, confirming the α conformation of PLLA (Zhang et al. 2005) in all nanocomposites. Carbonyl region band splitting was assigned to the crystallization of PLLA. In literature, this band is related to four conformations gt, gg, tg, and gt arising from interphase (Meaurio et al. 2006a, b). These conformations for semicrystalline PLLA were identified as follows: crystalline bands for gt appearing at 1760 cm^{-1} and 1758 cm^{-1} (splitting) and non-crystalline bands for, gg, tg, and gt appear at 1777 cm^{-1}, 1767 cm^{-1}, and 1759 cm^{-1}. In all the nanocomposites, bands appeared in gt conformation area suggesting crystalline phase because crystalline phase was mostly composed of gt conformation. Increase in integral intensity of this band indicated increase the crystallinity of the material after adding nanoparticles as reported in the cited literature (Szustakiewicz et al. 2018). In case of bands related to CH$_3$ and CH, however, we observed band broadening at 1133, 1086, and 1043 cm^{-1}. In case of nHA, these C–O–CH$_3$ peaks shifted to 1125, 1088, and 1020 cm^{-1}, while for nWH bands appeared at 1127, 1084, and 1037 cm^{-1}. Broadening of band at 1086 and 1043 cm^{-1} was assigned to the physical interaction occurring between

CH$_3$ of PLLA and PO$_4^{3-}$ of nHA or nWH. The broadening of this band could be attributed to the formation of hydrogen bonding (Raghavendran 2014). The peak intensity at 1753 cm^{-1} of C=O (PLLA) decreases, while the intensity at 1023, 629, 601 and 559 cm^{-1} increases proportional to the concentration of nHA added to the nanocomposites. This revealed that nHA had uniformly blended with PLLA (Zhao and Cai 2018).

In the third region from 970 to 850 cm^{-1} very interesting changes were observed. In PLLA–nHA, a shoulder appeared at 928 cm^{-1}, while band intensity at 958 cm^{-1} increased and band 872 cm^{-1} intensity decreased. For PLLA–nWH bands appeared at 985, 903 and 874 cm^{-1}. Mostly the band at 921 cm^{-1} is characteristic of 10^3 helix formation (Li et al. 2015) of PLLA and appears during the crystallization process, and the band at 957 cm^{-1} shrinks, while band at 867 cm^{-1} shifts to higher wavenumber and its integral intensity increases (Zhang et al. 2017). Our results showed that the peak of 867 cm^{-1} shifted to higher value in both nanocomposites and intensified in the case of PLLA–nWH. The band at 921 cm^{-1} in PLLA–nWH was masked by the PO$_4^{3-}$ bands expected at 989, whereas in PLLA–nHA the band appeared as shoulder near 921 cm^{-1}. For PLLA–nWH further bands were observed at 572 cm^{-1}, whereas in PLLA–nHA a band appeared at 600 cm^{-1} corresponding to PO$_4^{3-}$. Band intensity of these vibrations increased with the increasing concentration of the nanocomposite, suggesting the homogenous distribution of the nanoparticles throughout the PLLA matrix. Overall, results suggest that addition of nanoparticles increased the crystallinity of PLLA and conversion of any α' crystal structure to α crystal structure as corroborated by XRD results.

Morphology of the nanoparticles and nanocomposite films

The size and morphology of laboratory synthesized nWH and nHA were evaluated by SEM as shown in Fig. 3. The size of nWH was 17–23 nm as shown in Fig. 3a. The size of nHA was 23–40 nm and the shape was found to be spherical Fig. 3b. To visualize the homogenous distribution of different loading of nWH and nHA and the morphology of the PLLA (Fig. 3c) matrix, SEM images were obtained and are shown in Fig. 3d-i. The PLLA film was found to have a compact structure, and spherulitic structures were visible showing the crystalline nature of the PLLA. PLLA does not contain many side chain or bulky groups which could interfere with the packaging of the polymeric chains. When the nWH and nHA were added in lower concentrations, there was a clear formation of the porous structure, but at higher concentrations pores were less and smaller while some pit formation was seen. During the cryofracturing, breaking points of the film were the points of PLLA and nanoparticle
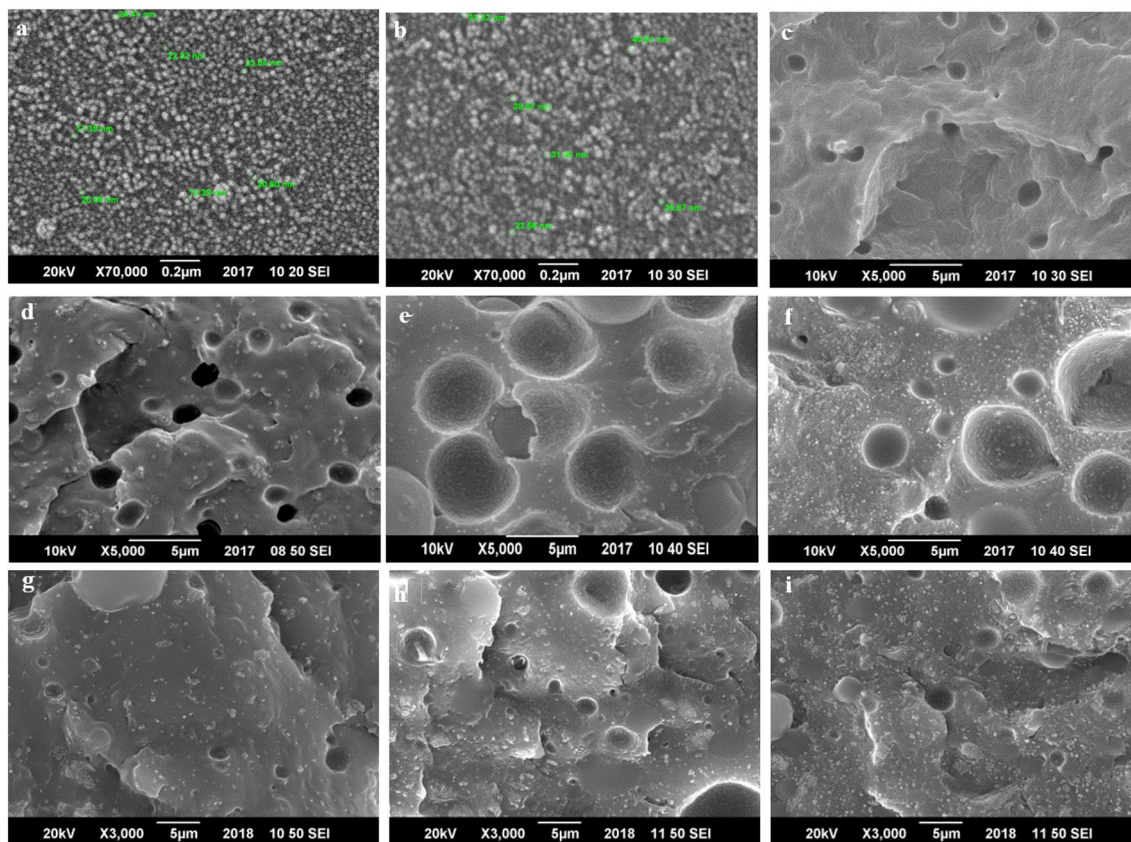
Fig. 3 SEM images of **a** nWH, **b** nHA, **c** PLLA, **d** PLLA–nHA1%, **e** PLLA–nHA5, **f** PLLA–nHA10% and %, PLLA–nWH1%, PLLA–nWH5%, and PLLA–nWH10%. Nanoparticle size, shape and their distribution in the polymer matrix are visible. With increasing con-centration, uniform distribution increases. PLLA matrix is more compact in case of WH; Mg^{2+} plays an important role in reinforcing the polymer matrix while in HA we have formation of pits and falls formation

interface. In nanocomposites, nanoparticles were distributed randomly and homogenously. At lower concentrations, there was homogeneous distribution of nanoparticles, while moving toward higher concentrations, the agglomeration started. We believed that when the ratio of the reinforcing agents to the polymer surpasses the critical value, hydrogen bodaing between the polymer and nanoparticles would cease to exist at higher concentrations, resulting in agglomeration at higher concentrations. A similar phenomenon was observed in case of PLLA/MCC/HA composites (Eftekhari et al. 2014). Agglomeration affected the mechanical properties and resulted in overall increased brittleness of the nanocomposites.

Tensile mechanical analysis

Tensile mechanical properties of nanocomposites depend on the overall crystallinity, homogenous dispersion of the nanofiller, physical attraction of the nanofiller and the polymer matrix, concentration of the nanofiller and the movement of the force from polymer to the reinforcing nanoparticles

(Alharbi et al. 2018; Bhasney et al. 2019). Stress–strain curves of PLLA and its nanocomposites with nWH and nHA are shown in Fig. 4a and b. Elongation at break (strain %) and ultimate tensile strength (UTS) at different loadings are presented in Fig. 4c and d, while Young's modulus values are presented in Table 1. Pristine PLLA has maximum tensile strength ~ 21 MPa, but fractured at the elongation value of 3.3% strain. PLLA–nWH and PLLA–nHA had higher strain percent values for elongation at break in comparison to pure PLLA, but UTS values decreased. nWH and nHA addition in PLLA resulted in strong and ductile PLLA than pristine PLLA. The reinforcing effect of the nanoparticles increased the elongation at break values of the polymer nanoparticle system. Among all nanocomposites, PLLA–nWH1% showed maximum ductility and appeared to be thew toughest material. Comparison of strain % values of elongation at break values at 1% nWH loading showed 403% and nWH 5% showed 315% increase, respectively, as compared to pure PLLA films. In case of PLLA–nHA, strain % values of elongation at break values showed a decreasing trend. Strain % values observed at different concentrations are 12.19% (1%
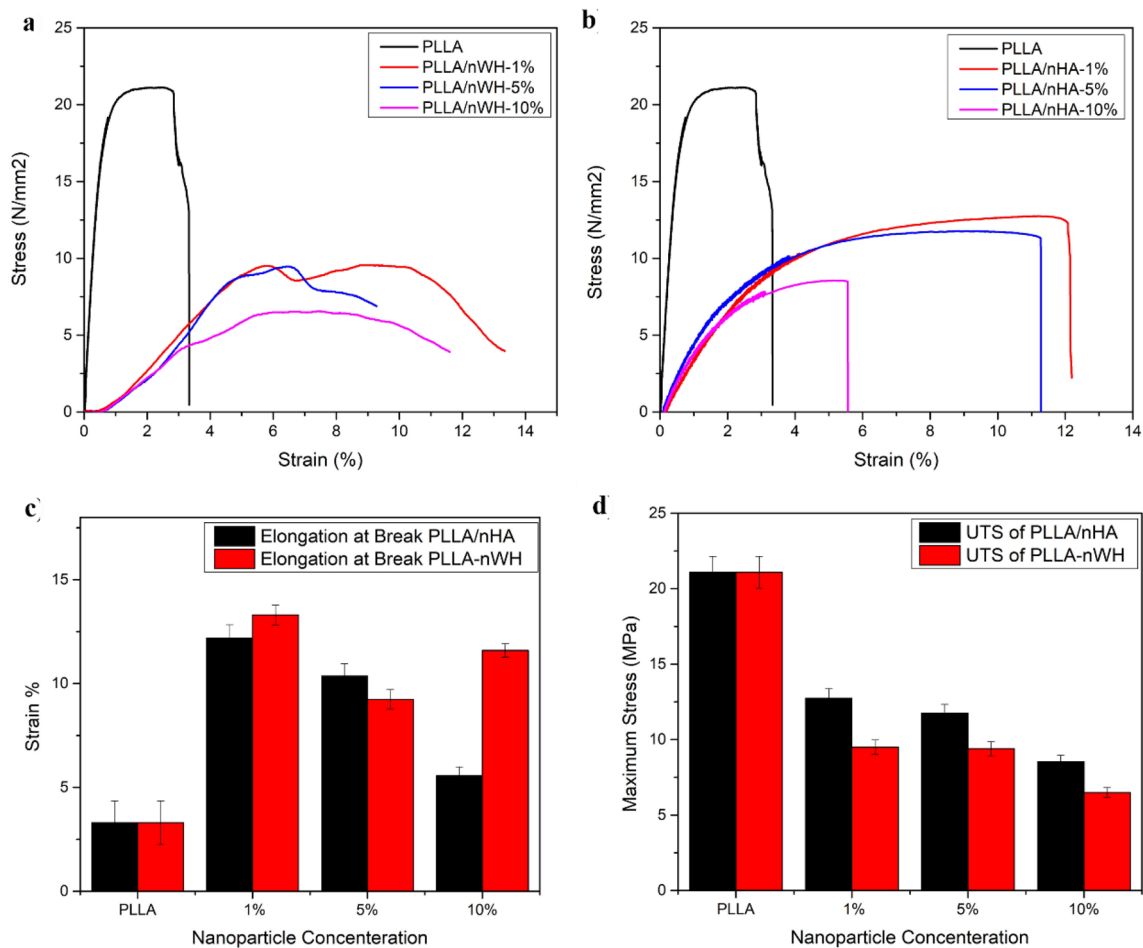
Fig. 4 a Tensile mechanical properties stress–strain graphs of PLLA–nHA and PLLA/nWH, **b** ultimate tensile strength of PLLA–nHA and PLLA/nWH, **c** Young's modulus of PLLA–nHA and PLLA/nWH, and **d** elongation at break of PLLA–nHA and PLLA/nWH (error bars: ± SD 0.05)

Table 1 Young's modulus of PLLA–nWH and PLLA–nHA nanocomposites

Percentage of nHA and nWA in PLLA	Young's modulus of PLLA–nHA (MPa)	Young's modulus of PLLA–nWH (MPa)
PLLA	571.65 ± 2.8	
1%	88 ± 5.4	103 ± 3.5
5%	104 ± 4.5	133 ± 6.1
10%	110 ± 6.2	148 ± 4.9

nHA), 10.37% (5% nHA), and 5.56% (10% nHA). Elongation at break values in 1% nHA (12.2%) were lower as compared to 1% nWH (13.3%), while at 10% loading the difference became more obvious where nHA strain% was 5.56 as compared to 10% nWHA11.59 strain %. Tensile strength values showed decreasing trend with increasing nanoparticle concentration. Among nanocomposites, PLLA–nHA1%

showed maximum tensile strength ~ 12.74 MPa. Ultimate strain percent value of PLLA with 1% nHA loading was 12.74 MPa and for 1% nWHA loading was 9.5 MPa. UTS values of PLLA/nHA were higher than that of PLLA–nWH. Decrease in UTS might be because of nanoparticle agglomeration in the polymer matrix, decreasing the reinforcing effect and leading to failure of the polymer at lower tensile strength values (Bhasney et al. 2019). Values of Young's modulus for the PLLA were found to be 572 MPa. In nHA-impregnated PLLA films, on increasing nHA content, there was an increasing trend of Young's modulus. For 1, 5 and 10% nHA in PLLA/COC-10, Young's modulus values were 103, 133 and 148 MPa, respectively. Values of Young's modulus in PLLA/nHA were lowered by 117%, 128%, and 134% in 1%, 5%, and10% PLLA/nHA as compared to PLLA–nWH. Cancellous bone requires the elastic modulus of 0.1–4.5 GPa, while that of cortical bone is 17 GPa (Hickey et al. 2015; Pitjamit et al. 2020). Depending upon these values of mechanical testing, the above-mentioned

films were a good candidate for the cancellous bone tissue engineering and dressing application. Specifically, these nanocomposites can be used in mechanically active area. Results revealed that the tensile mechanical properties of the polymers can be fine-tuned by changing the nanoparticle concentration in the nanocomposites. Two major factors causing the reinforcement are homogeneous dispersion and interfacial interaction of the polymer and filler. In our case both the factors contributed well to postponing the fracture time, resulting in higher strain %. The nanofillers were anchoring the polymer chains, thus leading to better mechanical properties than PLLA.

Antimicrobial activity

The antimicrobial activity of compounds was tested by Kirby–Bauer test, also known as the Zone of Inhibition. The antimicrobial activity of nanocomposites was checked against three different bacteria, (*E. coli*), (*S. aureus*) and (*L. monocytogenes*), as shown in Fig. 5. Gentamicin was used as the positive control, while the polymer system acted as a negative control. No inhibition zone was found for PLLA (Davachi et al. 2016), indicating no antibacterial potential of the PLLA. With 1–5% loading of nanoparticles in PLLA/nHA and PLLA/nWH, there was no significant antibacterial activity for the three bacteria, owing to very compact packing of the nanoparticles inside the PLLA matrix as indicated by SEM. Surprisingly, at 10% concentration, nanocomposites displayed significant response to bacteria as shown in Fig. 5a except with *E. Coli* which is Gram (–). The diameter of zone of inhibition (ZI) is shown in Fig. 5b. No inhibition zone against *E. coli* was observed for nanoparticle addition in PLLA, while for *S. aureus* PLLA–nHA10% showed very small ZI, while ZI values increased in case of PLLA–nWH10%. PLLA–nWH10% had maximum ZI for *L. monocytogenes* (9.4 mm) (Chandran et al. 2020). These results show that PLLA with 10% loading of nanoparticles of WH had a wide range in vitro activity against Gram-negative and Gram-positive Gram-negative bacteria with high activity against Gram-positive bacterial (Davachi et al. 2016; Davoodi et al. 2016). The reason for the largest zone of inhibition of Gram (+) bacteria strain could be credited to the absence of an outer layer membrane on the bacterial cell wall, whereas the presence of a thick outer layer of lipid membrane and lipopolysaccharides protect the Gram (−) bacteria from antimicrobial compounds (Akindoyo et al. 2019; Hassan and Sultana 2017) (Ou and Hsu 2007).

Swelling analysis

The surface properties of the material can be analyzed by swelling analysis (Nazir et al. 2021b; Nazir and Iqbal 2020). Swelling properties define the diffusion, surface properties

and mass transfer properties of the materials to be used as tissue engineering scaffold. Swelling properties of the nanocomposites with PBS buffer over 30 days' time are shown in Fig. 6a. PLLA had the lowest swelling ratio 9.8 ± 1.05 as compared to all composites (Peng et al. 2016). Low swelling ratio of the PLLA is because of the crystalline nature of PLLA having least spaces for the water to penetrate and be accommodated. Swelling ratios of PLLA increased by the addition of the nanoparticles. The increase in swelling behavior was owing to accumulation of water molecules by interacting with PO_4^{3-} and HPO_4^{1-} present in nWH and nHA through hydrogen bonding (as shown in FTIR). Interestingly, among nanocomposites, swelling ratios decreased with increasing weight loading of nanoparticles from 1 to 10%. PLLA having nHA had higher swelling ratios as compared to nWH at all concentrations. This might be because the small size and better dispersion of nWH provided the PLLA chains an anchoring and nucleation site. The network density increased, thereby reducing the swelling ratios. From day 1 to day 30, nHA1% swelling ratio increased by 104%, nHA5% increased by 106% and for nHA10% swelling ratio increased by 93%. From day 1 to day 30, nWH1% swelling ratio increased by 98%, nWH5% increased by 96% and for nWH% swelling ratio increased by 90%. From SEM images it was clear that the PLLA–nHA nanocomposites at lower concentration had pores, while the PLLA–-nWH had compact structure (Oyama 2020). Swelling ratios increased dramatically for the first 24 h, then very less addition of water was observed till day 14, and after that it reached at equilibrium. nWH and nHA were hydrophilic in nature and thus they increased the hydrophilic properties of the PLLA (Wang et al. 2020; Kim et al. 2019; Kumar et al. 2020). Moreover, the addition of the nanoparticles also affected the arrangement of PLLA polymeric network increasing crystallinity as indicated by XRD. These results suggest that by changing the nanoparticle concentration, we can fine-tune the swelling properties of the nanocomposites for bone tissue engineering.

Enzymatic degradation analysis

The degradation profile of the PLLA nanocomposites over 48 days was evaluated for bone tissue engineering applications (Danoux 2014; Shuai et al. 2021) as shown in Fig. 6b. Degradation rate is important, because it helps to understand that the time during the scaffold will degrade and meanwhile the new bone is regenerated in its place. During incubation with collagenase type II in a humidified incubator, the degradation rate of PLLA increased with respect to time especially in case of nanocomposites (Gunja and Athanasiou 2010; Izadpanahi et al. 2018). Enzymatic degradation occurred sooner and was imperative as compared to the hydrolytic degradation for tissue engineering appliance.

(a)

(b)
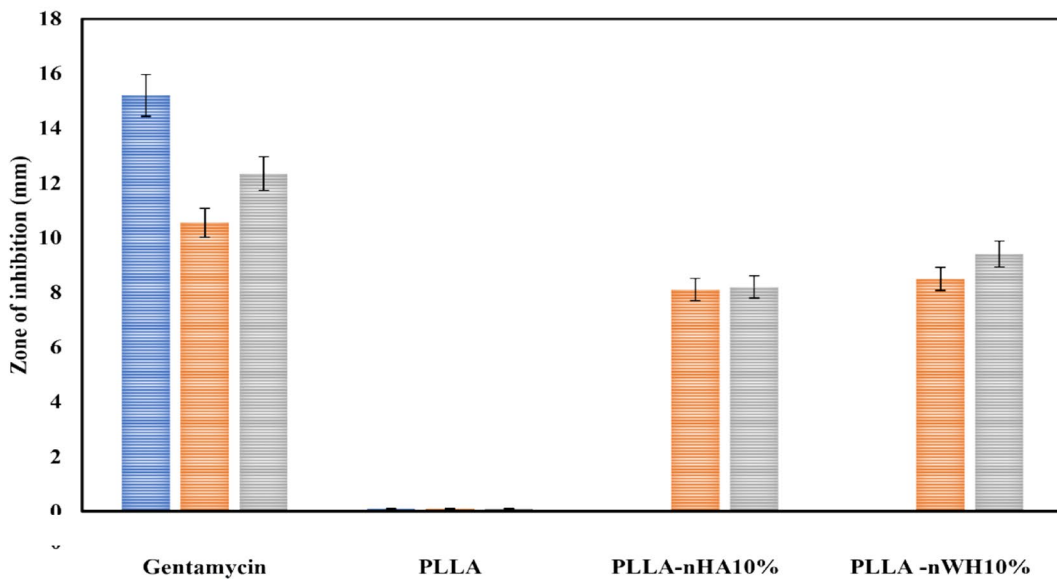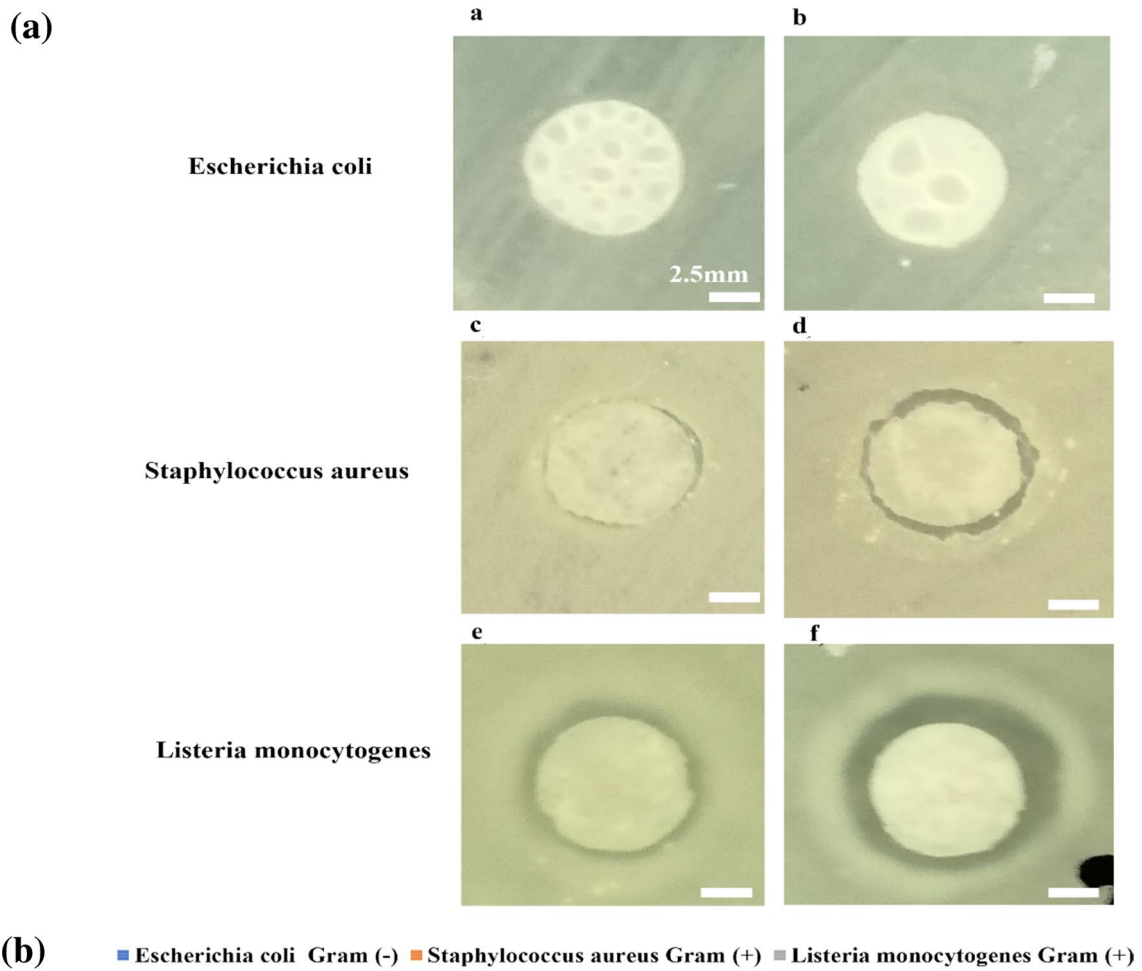
Fig. 5 **a** Antimicrobial activity of PLLA/nHA10% (**a**, **c**, **e**) and PLLA/nWH10% (**b**, **d**, **f**), with *E. Coli*, *Staphylococcus aureus* and *Listeria monocytogenes*. **b** Zone of inhibition. Data are statistically significant (error bars: ± SD, *$p \leq 0.05$, **$p \leq 0.01$, and ***$p \leq 0.001$)
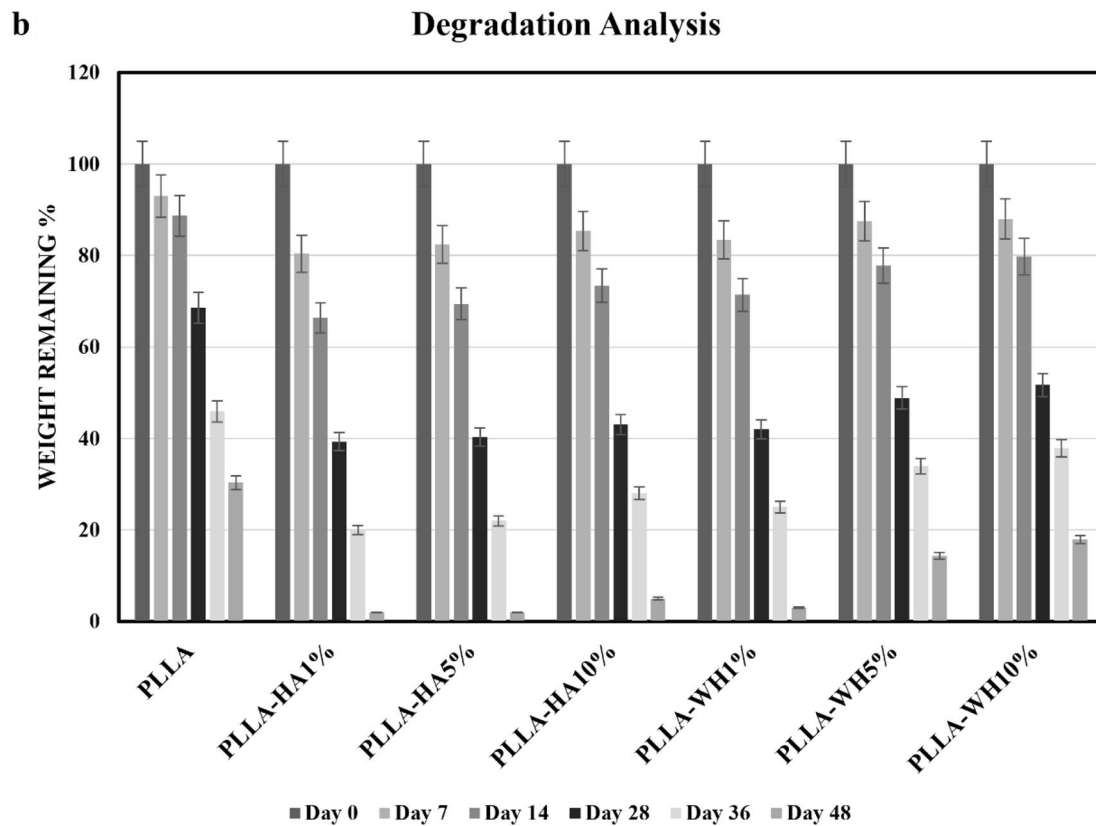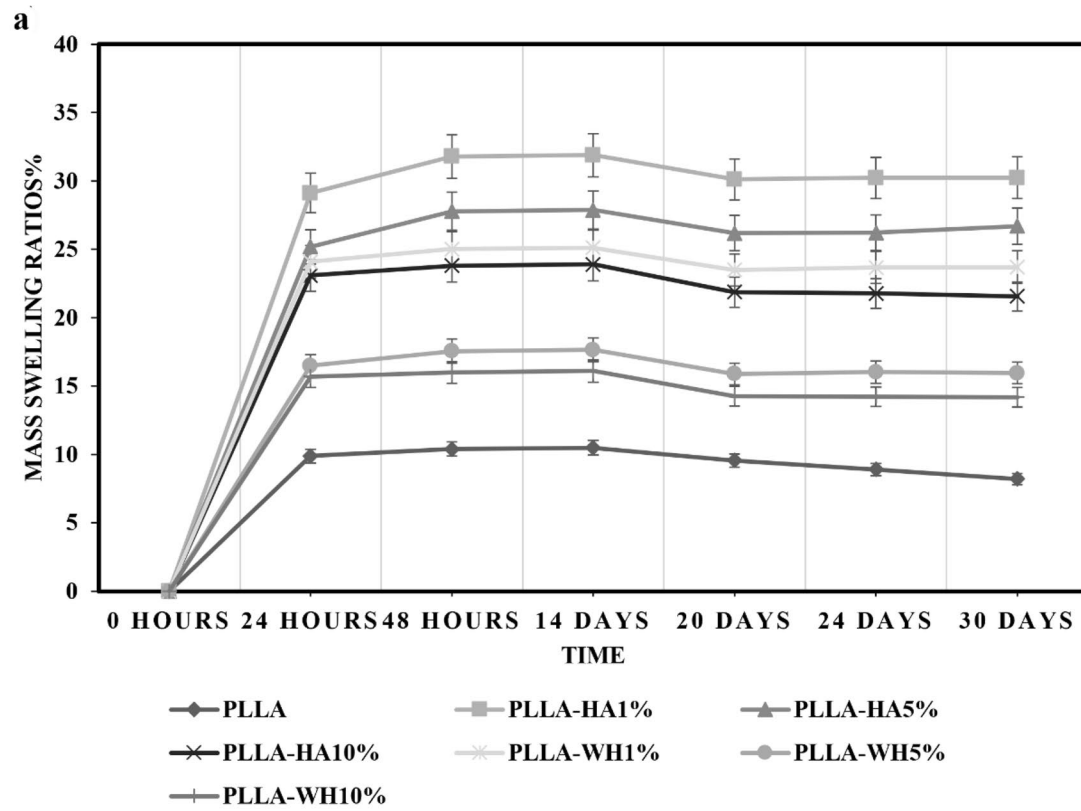
Fig. 6 **a** Mass swelling ratios of the nanocomposites in PBS. **b** Collagenase type II enzymatic degradation of the nanocomposites

PLLA is a polyester and is susceptible to enzymatic degradation, and also the degradation product of PLLA is acidic in nature (Nazir et al. 2021a). After 7 days, the remaining weight percent of PLLA was 93%, while after 48 days only 30% PLLA was left. Moreover, upon increasing the concentration of nanoparticles, the degradation rate of PLLA decreased. The maximum degradation rate was observed for blends containing 1% HA; 80.4% weight was observed after 7 days and reduced to only 2% after 48 days (Díaz et al. 2014). Interestingly, a similar trend was observed for nanocomposites containing PLLA–nWH. In case of nanocomposites, maximum degradation rate was observed for 1% nWH, with 83.4% after 7 days, reduced to 3% after 48 days (Díaz et al. 2019). Decrease in the degradation of PLLA in nanocomposites was attributed to structural change in nanocomposites by making the material denser and compact than PLLA to interact with chemical factors.

Cell culture

Cell viability, adhesion, and proliferation profiles are very important to study, as these determine the binding ability of the cells with the scaffold which is very crucial for proper cell functioning. Cell adhesion is usually linked to cellular function and tissue integration, whereas cell proliferation is linked to new bone creation due to cell multiplication (Nazir et al. 2021a). Therefore, better cell adhesion and proliferation would result in a large mass of bone tissue around the scaffold. In the present study, for the better understanding of the in vitro interaction of cell with nanocomposites, two cell lines, NIH3T3 and MC3T3-E1, were cultured on the surface of the nanocomposites. Cell viability, adhesion, and proliferation by PrestoBlue, LIVE/DEAD assay fluorescence and actin and DAPI staining on the surface of the PLLA–nHA and PLLA–nWH composites are shown in Figs. 7, 8, 9 and 10.

PrestoBlue cell viability indicator was used to check the reducing power of living cells to quantitatively measure the proliferation of cells. Cell viability by using PrestoBlue for 1, 3, and 7 days for NIH3T3 and MC3T3-E1 are shown in Fig. 7e and f. Interestingly, on the first day, nanocomposites showed almost similar growth pattern with cells attaching to the surface of the nanocomposites. Nonetheless, after that, all PLLA showed ~ 93% cell viability for both cell lines on day 3. Nanocomposite films PLLA–nWH10% showed 96.2% for NIH3T3 and 96–97% for MC3T3-E1 cells on day 3 (Fig. 7a, b), while PLLA–nHA10% was further increased to 94% for NIH3T3 and 96% for MC3T3-E1 cells on day 3. These results have been represented by taking as 100% the value of control cells without treatments and subtracting the values of media alone without cells with PrestoBlue. On day 7, PLLA–nWH at 1% showed 97% cell viability, whereas at 10%, 98% and in PLLA–nHA 1% had 94% cell viability and

10% had 96% for MC3T3-E1 cell lines. In case of NIH3T3, all nanocomposites had more than 94% cell viability. It can be inferred from the given cytocompatibility results that there was no compromise on biocompatibility and it is according to international standards of ISO 10993-5:2009 (Nosrati 2020a; Passos et al. 2016).

Cell density variation was measured by counting cells after 1, 3, and 7 days as shown in Figs. 7c, d and 10. The number of DAPI-stained cells per fixed area determines the cell density. These results show that when the concentration of nanoparticles was increased up to 10 wt%, increase in the cell attachment was observed which can be attributed to the surface properties and suitable nanocomposite roughness. This indicates that nHA and nWH reinforcement in PLLA provided additional osteogenesis and osteoinduction to the scaffolds (Nosrati 2020a; Zhu et al. 2019). From Fig. 7e and f, it is clear that cells have proliferated dramatically on the composites having nWH as compared to nHA nanocomposites for the 7 days cell culture. In literature, similar tests have been performed for measuring proliferation (Ain et al. 2017; Ain and Khan 2018).

From the cell orientation and growth pattern of MC3T3-E1 in Fig. 9, it can also be observed addition of different concentrations of nHA and nWH provided the site of attachment to the cells. Moreover, the cells were also show higher compatibility and growth with the nanocomposites with higher mechanical properties. In a previous study, PLLA blends (Nazir et al. 2021a) demonstrated potential as a biocompatible material with favorable interactions innate to the properties of parent materials. Here, osteoconduction was introduced by the incorporation of nWH and nHA in this blend, while in case of WH cell attachment proliferation and cell viability were enhanced because of the Mg^{2+} ions as reported (Hickey et al. 2015; Hickey et al. 2014; Hickey 2014). A similar phenomenon was found in our results: Mg^{2+} ions present in WH nanocomposites favored cell attachment and proliferation.

Figures 8 and 9 represent the LIVE/DEAD assays for NIH3T3 and MC3T3-E1, respectively. On day 1, the seeded cells presented noteworthy cell adhesion on the surface of nanocomposites. There was an increasing amount of cell growth attached onto the surface of the scaffolds having nWH in comparison to nHA because the polymer surface was hydrophobic, while the insertion of both nanoparticles into these scaffolds increased the hydrophilicity of the system. It was evident that in both kinds of nanocomposites, increasing the concentration of the nHA from 1 to 10% accelerated cell proliferation by 10- to 30-fold from day1 to day 7. On day 7, improved proliferation rate was observed due to the cell division, good morphology, and interconnected network. Cell adhesion morphology and proliferation of MC3T3-E1 cells with nanocomposites were better as compared to the NIH3T3 cell lines. Moreover, MC3T3-E1
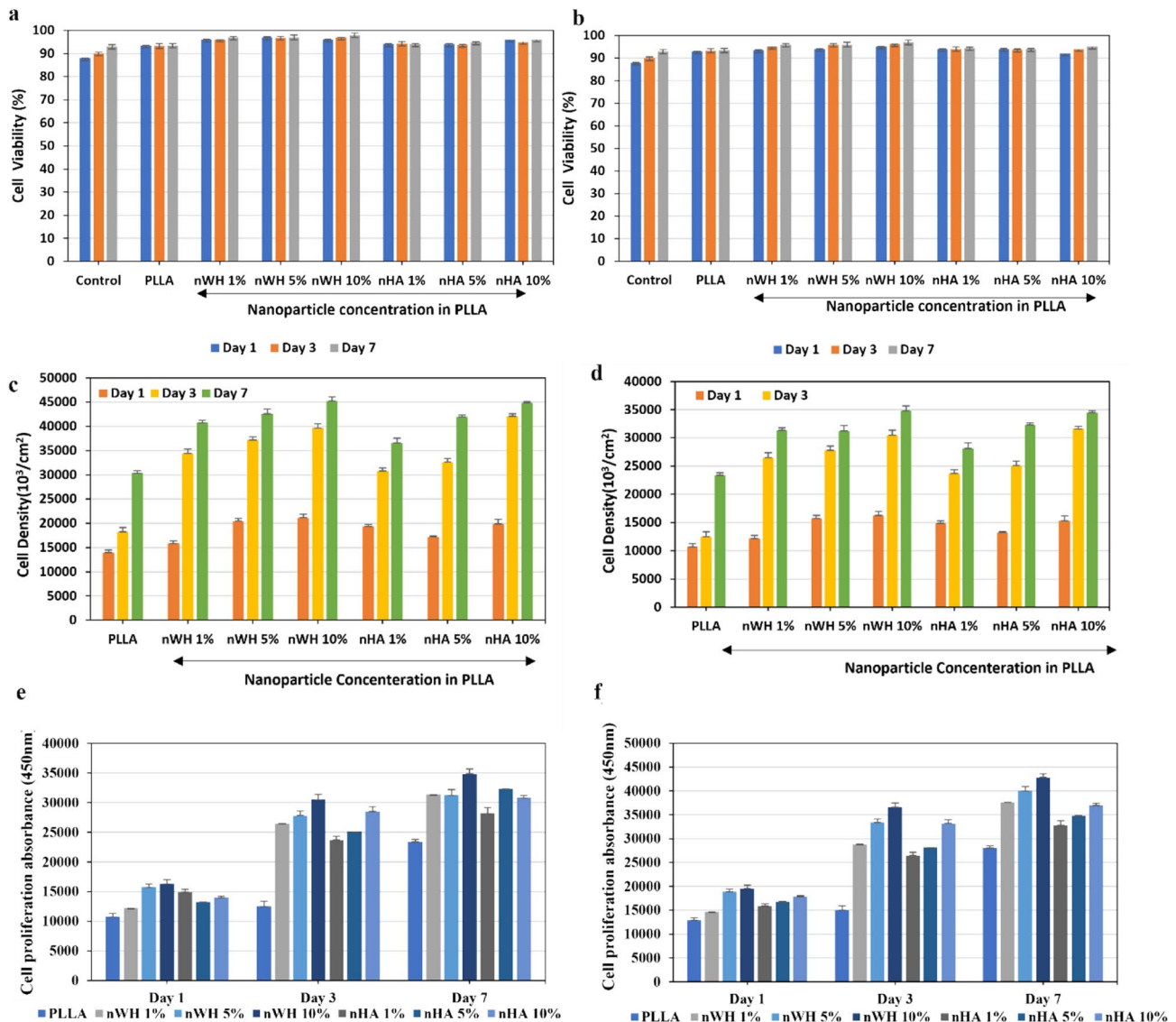
Fig. 7 The calculation of **a** cell viability of NIH3T3, **b** cell viability of MC3T3-E1, **c** cell density of NIH3T3, **d** cell density of MC3T3-E1, **e** proliferation of NIH3T3, **f** proliferation of MC3T3-E1 for day 1, 3, and 7 days. Data are statistically significant (error bars: $\pm$ SD, *$p \leq 0.05$, **$p \leq 0.01$, and ***$p \leq 0.001$)

cell density rose eight times on PLLA–nWH10% as compared to PLLA–nHA as shown in Fig. 9 for day 7. Cell density was determined based on live/dead cells by employing image J software. For 1, 3, and 7 days, cell viability is expressed as a proportion of living cells to the total number of cells exposed, as illustrated in Fig. 7c, and d. The ANOVA and estimated results as shown in Fig. 7 show that the cells were proliferating at a very high rate in case of PLLA/nWH. In comparison to PLLA–nHA, PLLA–nWH exhibited increased cytocompatibility at all WH loadings and its surface was found to be highly populated with cells. Cell density was found more profound in case of MC3T3-E1 cells as compared to NIH-3T3 cells. Although there was no

substantial change in the morphology in all the nanocomposites of PLLA–nWHA when weighed against PLLA–nHA, but as cells were influenced by their surroundings and their mechanical cues, the cellular function was influenced by PLLA–nWHA positively (Yang et al. 2020).

DAPI staining and F-actin assays were carried out to examine the morphologies along with proliferation of the cells as shown in Fig. 10. Cell counting found for the duration of cell culture along with image analysis by F-actin and DAPI validates the PrestoBlue analysis (Chakrapani et al. 2017; Qi et al. 2015). Cell viability in PLLA–nWH was increased by fivefold in case of NIH3T3 and sixfold in case of MC3T3-E1. Furthermore, in comparison to pure
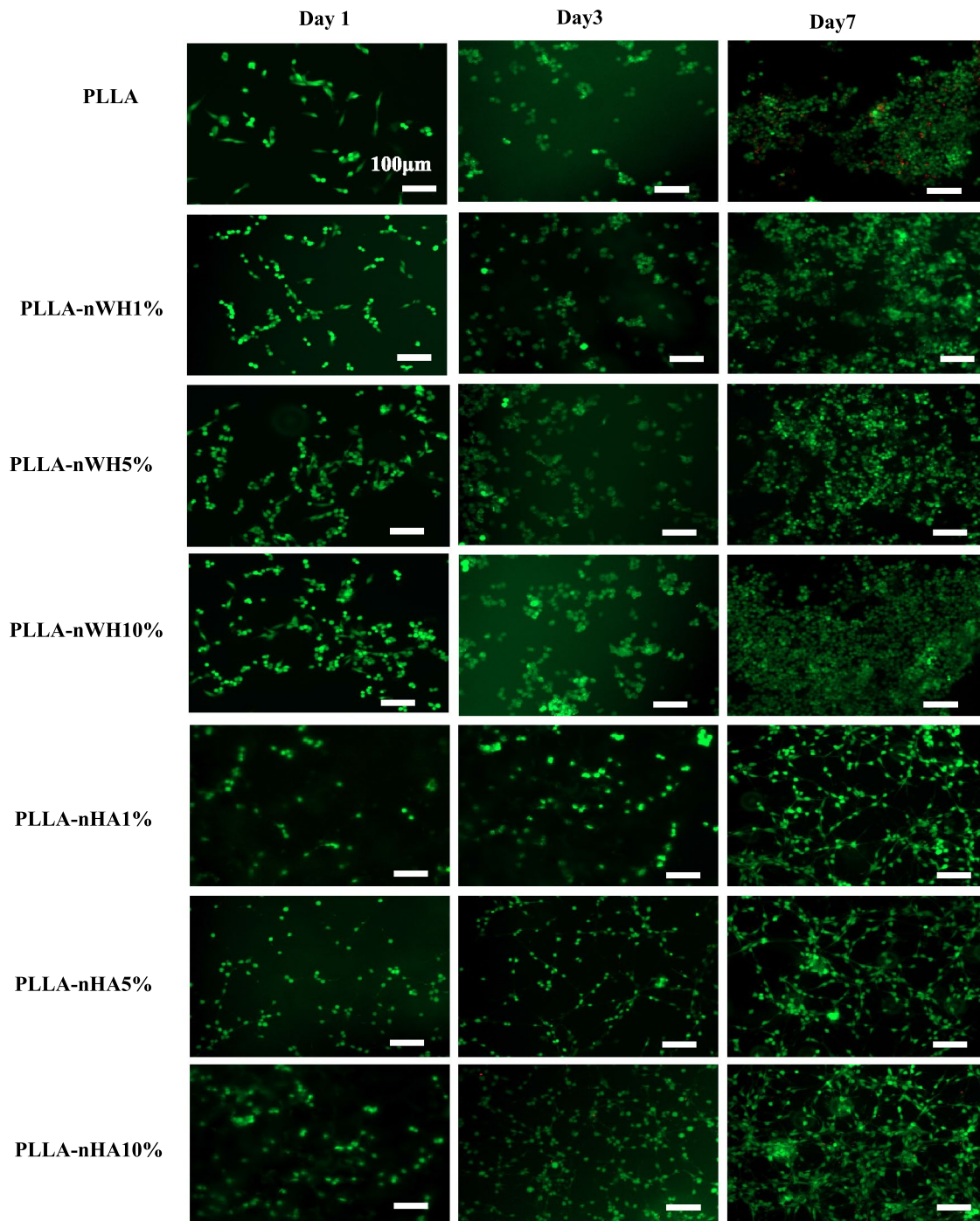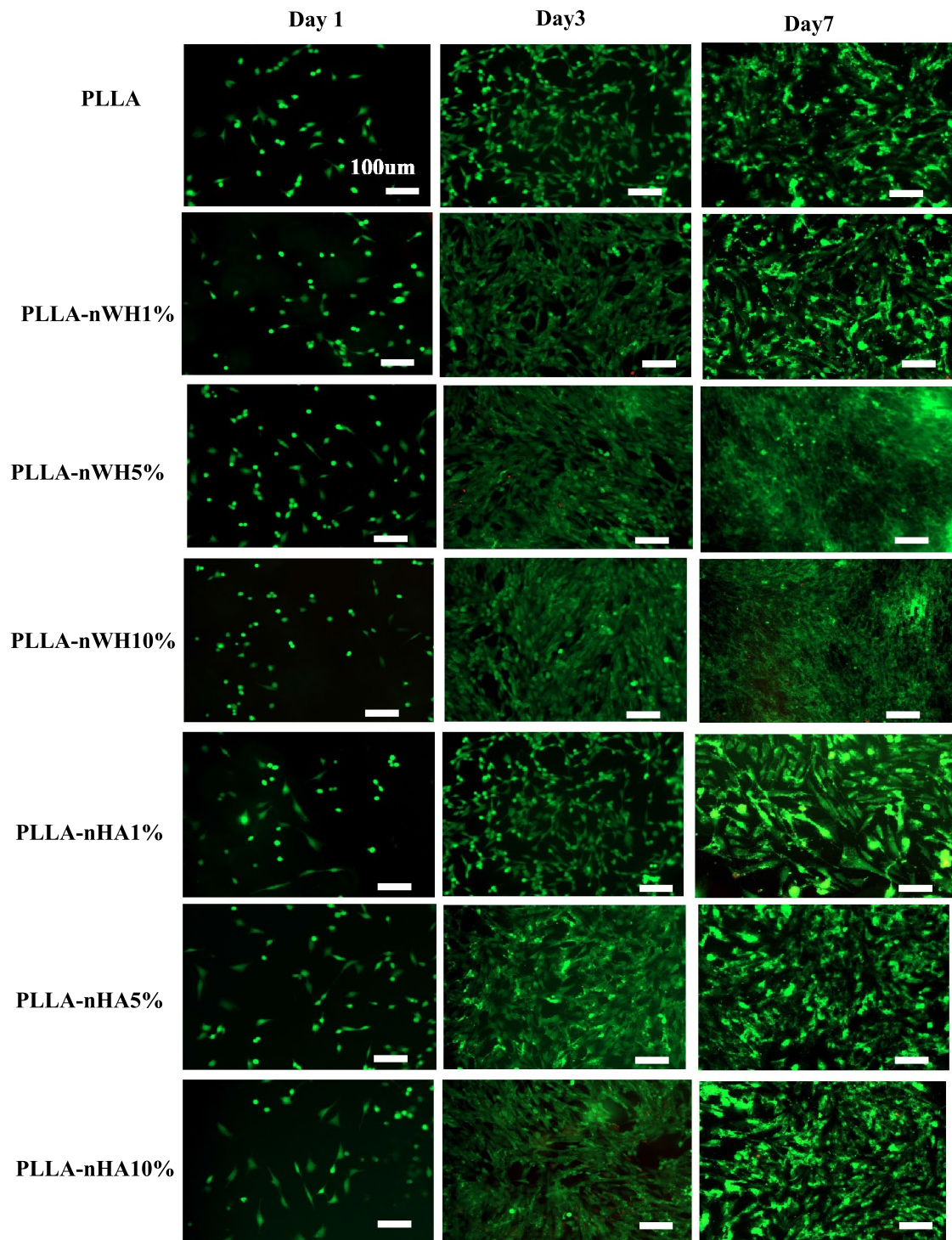
Fig. 8 LIVE/DEAD viability assay of fibroblast NIH3T3 cultivated onto pure PLLA, PLLA–nWH, and PLLA–nHA blends for day 1, 3, and 7 for which the scale bar is set at 100 μm. On day 1, PLLA–nWH surface shows decent adhesion of cells, followed by development of interconnected network on day 3. On day 7, cells are grown into mul-

tilayer displaying good cytocompatibility. When live cells are stained with calcein AM, they show green fluorescence; however, when dead cells are stained with ethidium homodimer, they show red fluorescence

PLLA–nHA cells, anchorage in the PLLA–nWH blends was with long distinct filopodia. When PLLA–nWH were scrutinized under a microscope, formation of focal adhesion was witnessed on day 2. Similar results were observed

by Zhou et al. in during comparing whitlockite/chitosan and hydroxyapatite/chitosan for bone regeneration (Zhou et al. 2017).

Fig. 9 LIVE/DEAD viability assay of fibroblast MC3T3-E1 cultivated onto pure PLLA, PLLA–nWH, and PLLA–nHA blends for days 1, 3, and 7, for which the scale bar is set at 100 μm. On day 1, PLLA–nWH surface shows decent adhesion of cells, followed by development of interconnected network on day 3. On day 7, cells are grown into multilayer displaying good cytocompatibility. When live cells are stained with calcein AM, they show green fluorescence; however, when dead cells are stained with ethidium homodimer, they show red fluorescence
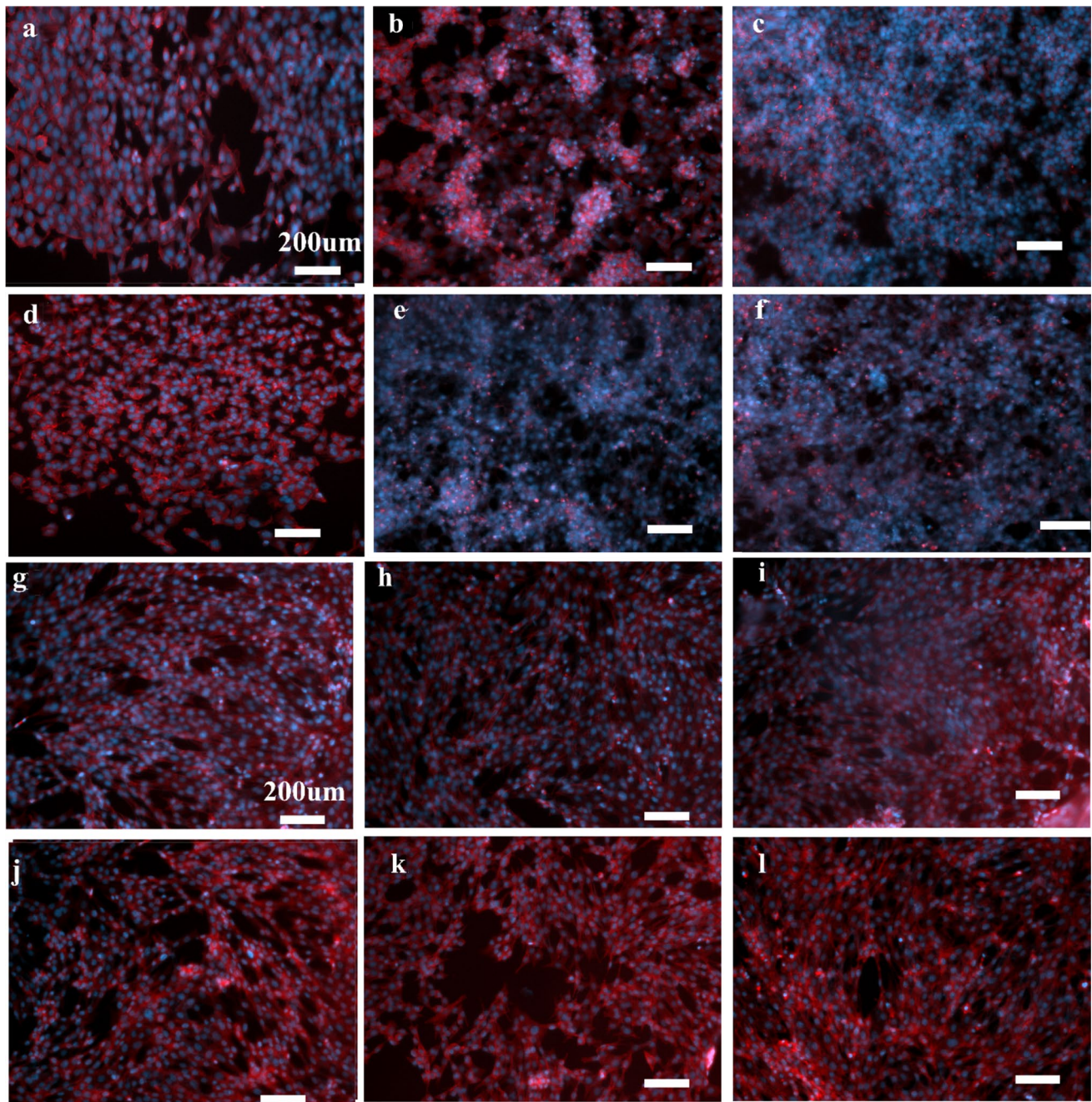
Fig. 10 DAPI and F-actin for NIH-3T3 (**a–e**) and MC3T3-E1 (**f–k**) cultivated onto PLLA, PLLA–nHA and PLLA–nWH PLLA–nHA for day 7. Here, the scale bar is set at 200 μm. DAPI characterized nuclei show blue fluorescence, while F-actin exhibits red fluorescence. Nuclear morphology illustrated by DAPI promotes growth of NIH-3T3 and MC3T3-E1 nuclei in a very high number, which puts forward the notion of increased cytocompatibility of the cell line with the PLLA–nWH blends. Cells developed interconnection, well distinct orientation, and incredibly profound cytoskeleton which is verified by actin filaments images

Interaction between the scaffold and cells was observed due to cell adhesion, which further led to the proliferation. Cell adhesion was significantly affected by the nanocomposites' roughness, mechanical properties and swelling behavior of the scaffold significantly influence cell adhesion. The cytoskeleton of the cell shows that the cytoskeleton's filaments help in anchoring the surface of the scaffold, verifying that biocompatibility of the scaffold plays its part in cell proliferation and adhesion. Filopodia formation was more intense and more pronounced in case of MC3T3-E1 cells, because of the existence of the bone mineral nanoparticles. MC3T3-E1 cells formed a dense population on

PLLA–WH nanocomposites because of anchoring to the surface of the scaffold at the site of the nanoparticles. These results reveal that WH nanoparticles help in early bone formation and remodeling, leading to dense bone formation.

Cell size, growth and morphology propose that there was decent scaffold–surface interaction and good surface protein, which was corroborated by F-actin and DAPI results as shown in Fig. 10. In contrast to cell proliferation, which depends on hydrophobic surface, cell adhesion was preferred with the hydrophilic surface. nHA and nWH inside the polymer system and onto the polymer surface assist in the cell adhesion due to the swelling, whereas the polymer system's hydrophobicity helps in the proliferation (Zhang et al. 2021). An ideal combination and balance of the hydrophobicity and hydrophilicity is important. Therefore, WH having smaller size and better dispersion in the PLLA–nWH system had more proliferation as compared to PLLA–nHA. Mechanically strong materials have higher cell viability and proliferation as compared to the mechanically weak materials (Wang et al. 2021). It has been proven in the literature that both the chemical structure and mechanical properties of the scaffold play vital part in not only in mineralization of bone cells, but also in differentiation and cell proliferation (Chen et al. 2012). Sensitivity and resulting response of cells to the mechanical properties such as rigidity of material's scaffold help in the regulation of their phenotypes along with a growing trend of cells to match the native tissue in the area of mechanical properties (Nazir et al. 2021b; Nabavinia et al. 2019; Alizadeh Sardroud et al. 2017). Uniform distribution of nWH in the polymer matrix and on the surface, as shown in the SEM, brings about a change in the surface structure providing site of adhesion to the cells. PLLA–nWH nanocomposites systems play a significant part in the regulation of cellular functions, which makes them an attractive alternative to the soluble supplements and growth factors as they are both expensive and carcinogenic (Kraehenbuehl et al. 2008). Several studies suggest that the hard materials help in differentiation (Alizadeh Sardroud et al. 2017; Sharma et al. 2016; Dyke et al. 2012). Polyethylene glycol-containing scaffolds show no mineralization and had lesser modulus values which makes them an unsuitable material for hard mineralized bone, as hard mineralized bone requires high modulus in contrast to collagenous bone. In the same way, our results depict the nanocomposite system stiffness detections by cells and improvement in cell physiology upon the closeness of modulus values of the scaffold to the native bone tissue (Chatterjee et al. 2010). These results propose that the nanocomposites of PLLA/nWH have a better association between structure, swelling, degradation, mechanical, antibacterial activity, and cytocompatibility for applications in tissue engineering as compared to PLLA–nHA and have

suitable properties to be used as scaffold material for bone tissue engineering. Physical contact between the cells and scaffold was increased by using nWH, because of the formation of the cellular bridges formed by the cytoplasmic channels (filopodia). Physical contact between cells helped in increased transfer of signaling and molecular moieties. Filopodia facilitate cellular interaction necessary for proliferation and differentiation.

Mineralization studies

Mineralization studies at day 14 were done using Alizarin red assay. Clear nodule formation indicative of the mineralization appeared at day 14 as shown in Fig. 11. PLLA having nWH had increased nodule and filopodia formation in comparison to PLLA/nHA. These outcomes are reinforced by the LIVE DEAD and actin and DAPI staining. In case of PLLA/nWH 10%, we observed twofold increase in the mineralization as compared to PLLA/nHA at the same weight percentage. These results propose that nanocomposites of PLLA/nWH not only help in the proliferation and adhesion of NIH-3T3 cells, but also assist in the mineralization of MC3T3-E1cells. It was clearly attested that PLLA/nWH has a great potential for bone tissue engineering scaffold and was competent as compared to PLLA/nHA. Wijnhoven I B have also reported that calcium phosphate-based biomaterials increase cellular bridge formation with human gingival mesenchymal stem cells (hGMSCs) (Wijnhoven et al. 2020).

Conclusion

nHA and nWH nanoparticles were successfully laboratory synthesized and characterized by FTIR, PXRD and SEM. PLLA–nHA and PLLA–nWH composites were successfully prepared by the physical blending method. Different concentrations from 1 to 10% nHA and nWH were incorporated intp PLLA and the two systems were compared. SEM images displayed uniform distribution of nHA and nWH inside the matrix of PLLA up to 10%. Fingerprint region of FTIR confirmed that with the addition, nanoparticle interfacial bonding between PLLA, nHA and nWH was observed. Moreover, the intensity of the band position confirmed that nWH increased the crystallinity of PLLA. Change in crystallinity was further validated by PXRD. XRD patterns and FTIR band positions, confirming that the crystallinity of PLLA transformed from PLLA α′ to PLLA α. Additionally, the crystallinity of blends increased with increasing nHA. Furthermore, the mechanical properties of nanocomposites exhibited enhancement of ductility of PLLA. PLLA nanocomposites exhibited enhancement of toughness by 403–315% (for 1–5% of nWH) as

Fig. 11 Alizarin red S staining of MC3T3-E1 showing the mineralization of cells. In this procedure, cells were first cultivated for 14 days followed by staining with Alizarin red S at 14 days to detect the mineralized nodule. Scale bar was 100 μm and after carrying out three independent trials data were presented
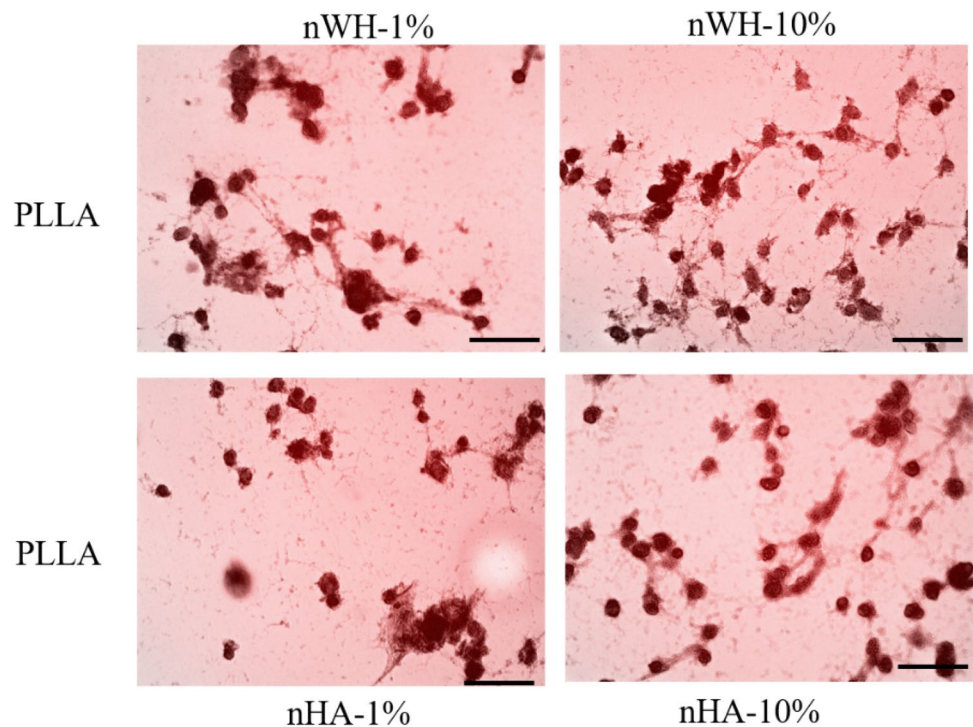
compared to pure PLLA. Nanocomposite PLLA–nWH had better degradation, swelling properties and cytocompatibility as compared to PLLA–nHA at different nanoparticle concentrations. Addition of nWH induced antibiotic potential in PLLA at 10 wt% loading of nWH against *Staphylococcus aureus* and *Listeria monocytogenes*. Interestingly, PLLA–nWH as compared to PLLA–nHA showed significant increase in cell viability and proliferation of fibroblasts NIH3T3 and MC3T3-E1. PLLA–nWH10% had 96% cell viability at day 7 for NIH3T3 and 98% for MC3T3-E1, while other nanocomposites had greater than 94% cell viability. Alizarin red assay for mineralization revealed two-fold increase in calcification at day 14 with PLLA–nWH as compared to PLLA–nHA. In short, this study reveals that PLLA–nWH had better mechanical properties, enhanced antibacterial activity and suitable cytotoxicity as compared to PLLA–nHA. Furthermore, by changing the nanoparticle concentration, we can fine-tune the scaffold properties for bone regeneration. Our studies revealed that PLLA–nWH can be a better potential biomaterial in comparison to PLLA–nHA, as a replacement of allografts/autografts for bone tissue engineering applications after in vivo studies.

Declarations

Conflict of interest The authors declare no conflict of interest.

References

Ain QU, Khan ANJPC (2018) Fabrication and characterization of bio-inspired polymer blends and hybrid composites based on collagen-type II, polyethylene glycol-dimethacrylate and hydroxyapatite. Polym Compos 39:E550–E560

Ain QU et al (2017) Enhanced mechanical properties and biocompatibility of novel hydroxyapatite/TOPAS hybrid composite for bone tissue engineering applications. Mater Sci Eng C 75:807–815

Akindoyo JO et al (2019) Synergized poly(lactic acid)–hydroxyapatite composites: biocompatibility study. J Appl Polym Sci 136(15):47400

Alharbi HF et al (2018) Fabrication of core-shell structured nanofibers of poly (lactic acid) and poly (vinyl alcohol) by coaxial electrospinning for tissue engineering. Eur Polym J 98:483–491

Alizadeh Sardroud H et al (2017) Barium-cross-linked alginate-gelatine microcapsule as a potential platform for stem cell production and modular tissue formation. J Microencapsul 34(5):488–497

Amin S et al (2015) Synthesis and characterization of nano hydroxyapatite using reverse micro emulsions as nano reactors. J Chem Soc Pak 37(1):79–85

Athanasoulia I-GI et al (2017) The effect of hydroxyapatite nanoparticles on crystallization and thermomechanical properties of PLLA matrix. Pure Appl Chem 89(1):125–140

Beltrán F et al (2016) Water-induced structural changes in poly (lactic acid) and PLLA-clay nanocomposites. Polymer 107:211–222

Bhasney SM et al (2019) Morphology and crystalline characteristics of polylactic acid [PLA]/linear low density polyethylene [LLDPE]/microcrystalline cellulose [MCC] fiber composite. Compos Sci Technol 171:54–61

Capitelli F et al (2021) Neutron and XRD single-crystal diffraction study and vibrational properties of whitlockite, the natural counterpart of synthetic tricalcium phosphate. Curr Comput-Aided Drug Des 11(3):225

Chakrapani VY et al (2017) Electrospun cytocompatible polycaprolactone blend composite with enhanced wettability for bone tissue engineering. J Nanosci Nanotechnol 17(4):2320–2328

Chandran RR et al (2020) Evaluation of whitlockite through conventional hydrothermal method and its in-vitro erythrocyte compatibility and antibacterial activity. In: AIP conference proceedings, AIP Publishing LLC

Chatterjee K et al (2010) The effect of 3D hydrogel scaffold modulus on osteoblast differentiation and mineralization revealed by combinatorial screening. Biomaterials 31(19):5051–5062

Chen YC et al (2012) Functional human vascular network generated in photocrosslinkable gelatin methacrylate hydrogels. Adv Funct Mater 22(10):2027–2039

Cheng H et al (2018) Synergistic interplay between the two major bone minerals, hydroxyapatite and whitlockite nanoparticles, for osteogenic differentiation of mesenchymal stem cells. Acta Biomater 69:342–351

Christy PN et al (2020) Biopolymeric nanocomposite scaffolds for bone tissue engineering applications–a review. J Drug Deliv Sci Technol 55:101452

Cooper MA et al (2013) Wopmayite, ideally Ca_6Na_3 Mn $(PO_4)_3$ $(PO_3OH)_4$, a new phosphate mineral from the Tanco Mine, Bernic Lake, Manitoba: description and crystal structure. Can Mineral 51(1):93–106

Danoux CB et al (2014) In vitro and in vivo bioactivity assessment of a polylactic acid/hydroxyapatite composite for bone regeneration. Biomatter 4(1):e27664

Davachi SM et al (2016) In-vitro investigation and hydrolytic degradation of antibacterial nanocomposites based on PLLA/triclosan/nano-hydroxyapatite. Polymer 83:101–110

Davoodi S et al (2016) Preparation and characterization of interface-modified PLA/starch/PCL ternary blends using PLLA/triclosan antibacterial nanoparticles for medical applications. RSC Adv 6(46):39870–39882

Díaz E et al (2014) In vitro degradation of PLLA/nHA composite scaffolds. Polym Eng Sci 54(11):2571–2578

Díaz E et al (2019) PLLA/nHA composite films and scaffolds for medical implants: in vitro degradation, thermal and mechanical properties. J Inorg Organomet Polym Mater 29(1):121–131

Doosti-Telgerd M et al (2020) Nanofibrous scaffolds containing hydroxyapatite and microfluidic-prepared polyamidoamin/BMP-2 plasmid dendriplexes for bone tissue engineering applications. Int J Nanomedicine 15:2633

Dyke JC et al (2012) An investigation of siloxane cross-linked hydroxyapatite–gelatin/copolymer composites for potential orthopedic applications. J Mater Chem 22(43):22888–22898

Eftekhari S et al (2014) Fabrication and characterization of novel biomimetic PLLA/cellulose/hydroxyapatite nanocomposite for bone repair applications. Mater Sci Eng C 39:120–125

Farokhi M et al (2018) Silk fibroin/hydroxyapatite composites for bone tissue engineering. Biotechnol Adv 36(1):68–91

Gieroba B et al (2021) Collagen maturity and mineralization in mesenchymal stem cells cultured on the hydroxyapatite-based bone scaffold analyzed by ATR-FTIR spectroscopic imaging. Mater Sci Eng C 119:111634

Gunja NJ, Athanasiou KA (2010) Effects of hydrostatic pressure on leporine meniscus cell-seeded PLLA scaffolds. J Biomed Mater Res Part A 92(3):896–905

Harb SV et al (2020) Hydroxyapatite and β-TCP modified PMMA-TiO_2 and PMMA-ZrO_2 coatings for bioactive corrosion protection of Ti_6Al_4V implants. Mater Sci Eng C 116:111149

Hassan MI, Sultana N (2017) Characterization, drug loading and antibacterial activity of nanohydroxyapatite/polycaprolactone (nHA/PCL) electrospun membrane. 3 Biotech 7(4):1–9

Hickey DJ (2014) MgO nanocomposites as antibacterial biomaterials for orthopedic tissue engineering. Northeastern University, Boston

Hickey DJ et al (2014) MgO nanocomposites as new antibacterial materials for orthopedic tissue engineering applications. In: 2014 40th Annual northeast bioengineering conference (NEBEC), IEEE

Hickey DJ et al (2015) Adding MgO nanoparticles to hydroxyapatite–PLLA nanocomposites for improved bone tissue engineering applications. Acta Biomater 14:175–184

Hu X, Zhang W, Hou D (2020) Synthesis, microstructure and mechanical properties of tricalcium phosphate–hydroxyapatite (TCP/HA) composite ceramic. Ceram Int 46(7):9810–9816

Izadpanahi M et al (2018) Nanotopographical cues of electrospun PLLA efficiently modulate non-coding RNA network to osteogenic differentiation of mesenchymal stem cells during BMP signaling pathway. Mater Sci Eng C 93:686–703

Jang HL et al (2014) Revisiting whitlockite, the second most abundant biomineral in bone: nanocrystal synthesis in physiologically relevant conditions and biocompatibility evaluation. ACS Nano 8(1):634–641

Jang HL et al (2015) Phase transformation from hydroxyapatite to the secondary bone mineral, whitlockite. J Mater Chem B 3(7):1342–1349

Jang HL et al (2016) In vitro and in vivo evaluation of whitlockite biocompatibility: comparative study with hydroxyapatite and β-tricalcium phosphate. Adv Healthc Mater 5(1):128–136

Jin Y-Z et al (2019) Whitlockite promotes bone healing in rabbit ilium defect model. J Med Biol Eng 39(6):944–951

Kaliannagounder VK et al (2021) Remotely controlled self-powering electrical stimulators for osteogenic differentiation using bone inspired bioactive piezoelectric whitlockite nanoparticles. Nano Energy 85:105901

Kanani AG, Bahrami SH (2010) Review on electrospun nanofibers scaffold and biomedical applications. Trends Biomater Artif Organs 24(2):93–115

Kaya I et al (2019) Three dimensional printing and biomaterials in the repairment of bone defects; hydroxyapatite PLA filaments. Turk J Med Sci 49(3):922–927

Kim HD et al (2017) Biomimetic whitlockite inorganic nanoparticles-mediated in situ remodeling and rapid bone regeneration. Biomaterials 112:31–43

Kim I et al (2019) Osteogenic effects of VEGF-overexpressed human adipose-derived stem cells with whitlockite reinforced cryogel for bone regeneration. Macromol Biosci 19(5):1800460

Klinkaewnarong J, Utara S (2018) Ultrasonic-assisted conversion of limestone into needle-like hydroxyapatite nanoparticles. Ultrason Sonochemistry 46:18–25

Kraehenbuehl TP et al (2008) Three-dimensional extracellular matrix-directed cardioprogenitor differentiation: systematic modulation

of a synthetic cell-responsive PEG-hydrogel. Biomaterials 29(18):2757–2766

Kumar S et al (2020) Enhanced mechanical properties and hydrophilic behavior of magnesium oxide added hydroxyapatite nanocomposite: a bone substitute material for load bearing applications. Ceram Int 46(10):16235–16248

Li S et al (2015) Structural changes and crystallization kinetics of polylactide under CO_2 investigated using high-pressure Fourier transform infrared spectroscopy. Polym Int 64(12):1762–1769

Meaurio E, López-Rodríguez N, Sarasua J (2006a) Infrared spectrum of poly (L-lactide): application to crystallinity studies. Macromolecules 39(26):9291–9301

Meaurio E et al (2006b) Conformational behavior of poly (L-lactide) studied by infrared spectroscopy. J Phys Chem B 110(11):5790–5800

Mohseni M et al (2018) Assessment of tricalcium phosphate/collagen (TCP/collagene) nanocomposite scaffold compared with hydroxyapatite (HA) on healing of segmental femur bone defect in rabbits. Artif Cells Nanomedicine Biotechnol 46(2):242–249

Mondal S et al (2020) Hydroxyapatite nano bioceramics optimized 3D printed poly lactic acid scaffold for bone tissue engineering application. Ceram Int 46(3):3443–3455

Muthiah Pillai NS et al (2019) Injectable nano whitlockite incorporated chitosan hydrogel for effective hemostasis. ACS Appl Bio Mater 2(2):865–873

Nabavinia M, Khoshfetrat AB, Naderi-Meshkin H (2019) Nano-hydroxyapatite-alginate-gelatin microcapsule as a potential osteogenic building block for modular bone tissue engineering. Mater Sci Eng C 97:67–77

Nazeer MA, Yilgör E, Yilgör I (2017) Intercalated chitosan/hydroxyapatite nanocomposites: promising materials for bone tissue engineering applications. Carbohydr Polym 175:38–46

Nazir F, Iqbal M (2020) Synthesis, characterization and cytotoxicity studies of aminated microcrystalline cellulose derivatives against melanoma and breast cancer cell lines. Polymers 12(11):2634

Nazir F et al (2021a) Fabrication of robust poly L-lactic acid/cyclic olefinic copolymer (PLLA/COC) blends: study of physical properties, structure, and cytocompatibility for bone tissue engineering. J Mater Res Technol 13:1732–1751

Nazir F et al (2021b) 6-deoxy-aminocellulose derivatives embedded soft gelatin methacryloyl (GelMA) hydrogels for improved wound healing applications: in vitro and in vivo studies 185:419-433

Nie W et al (2017) Three-dimensional porous scaffold by self-assembly of reduced graphene oxide and nano-hydroxyapatite composites for bone tissue engineering. Carbon 116:325–337

Nosrati H et al (2020a) Nucleation and growth of brushite crystals on the graphene sheets applicable in bone cement. Boletín de la Sociedad Española de Cerámica y Vidrio 2020. https://doi.org/10.1016/j.bsecv.2020.05.001.

Nosrati H et al (2020b) Statistical evaluation of nano-structured hydroxyapatite mechanical characteristics by employing the Vickers indentation technique. Ceram Int 46(12):20081–20087

Nosrati H et al (2020c) Gas injection approach for synthesis of hydroxyapatite nanorods via hydrothermal method. Mater Charact 159:110071

Nosrati H et al (2020d) Evaluation of argon-gas-injected solvothermal synthesis of hydroxyapatite crystals followed by high-frequency induction heat sintering. Cryst Growth Des 20(5):3182–3189

Oner FK, Alakent B, Soyer-Uzun S (2021) Effect of silane A-174 modifications in the structure, chemistry, and compressive strength of PLA-HAP and PLA-β-TCP biocomposites: toward the design of polymer-ceramic implants with high performance. ACS Appl Polym Mater 3(5):2432–2446

Ou C-F, Hsu M-C (2007) Preparation and characterization of cyclo olefin copolymer (COC)/silica nanoparticle composites by solution blending. J Polym Res 14(5):373–378

Oustadi F et al (2020) Genipin-crosslinked gelatin hydrogel incorporated with PLLA–nanocylinders as a bone scaffold: Synthesis, characterization, and mechanical properties evaluation. Polym Adv Technol 31(8):1783–1792

Oyama HT et al (2020) Environmentally safe bioadditive allows degradation of refractory poly (lactic acid) in seawater: effect of poly (aspartic acid-co-l-lactide) on the hydrolytic degradation of PLLA at different salinity and pH conditions. Polym Degrad Stab 178:109216

Passos MF et al (2016) PHEMA-PLLA semi-interpenetrating polymer networks: a study of their swelling kinetics, mechanical properties and cellular behavior. Eur Polym J 85:150–163

Pavia FC et al (2018) Preparation, characterization and in vitro test of composites poly-lactic acid/hydroxyapatite scaffolds for bone tissue engineering. Int J Biol Macromol 119:945–953

Peng H et al (2016) Synthesis, swelling, degradation and cytocompatibility of crosslinked PLLA-PEG-PLLA networks with short PLLA blocks. Eur Polym J 84:448–464

Pitjamit S et al (2020) The possibility of interlocking nail fabrication from FFF 3D printing PLA/PCL/HA composites coated by local silk fibroin for canine bone fracture treatment. Materials 13(7):1564

Qi C et al (2015) Porous microspheres of magnesium whitlockite and amorphous calcium magnesium phosphate: microwave-assisted rapid synthesis using creatine phosphate, and application in drug delivery. J Mater Chem B 3(39):7775–7786

Raghavendran HRB et al (2014) A comparative study on in vitro osteogenic priming potential of electron spun scaffold PLLA/HA/Col, PLLA/HA, and PLLA/Col for tissue engineering application. PLoS One 9(8):e104389

Raghavendran HRB et al (2021) The functionalization of the electrospun PLLA fibrous scaffolds reduces the hydrogen peroxide induced cytokines secretion in vitro. Mater Today Commun 26:101812

Righetti MC et al (2017) Contribution of the rigid amorphous fraction to physical ageing of semi-crystalline PLLA. Polymer 125:241–253

Righetti MC, Delpouve N, Saiter A (2018) Physical ageing of semi-crystalline PLLA: role of the differently constrained amorphous fractions. In: AIP conference proceedings, AIP Publishing LLC

Rodenas-Rochina J et al (2015) Effects of hydroxyapatite filler on long-term hydrolytic degradation of PLLA/PCL porous scaffolds. Polym Degrad Stab 119:121–131

Sharma C et al (2016) Fabrication and characterization of novel nano-biocomposite scaffold of chitosan–gelatin–alginate–hydroxyapatite for bone tissue engineering. Mater Sci Eng C 64:416–427

Shuai C et al (2021) Accelerated degradation of HAP/PLLA bone scaffold by PGA blending facilitates bioactivity and osteoconductivity. Bioact Mater 6(2):490–502

Silver I, Murrills R, Etherington D (1988) Microelectrode studies on the acid microenvironment beneath adherent macrophages and osteoclasts. Exp Cell Res 175(2):266–276

Sroka-Bartnicka A et al (2017) Structural transformation of synthetic hydroxyapatite under simulated in vivo conditions studied with ATR-FTIR spectroscopic imaging. Spectrochim Acta Part A Mol Biomol Spectrosc 171:155–161

Szustakiewicz K et al (2018) Femtosecond laser-induced modification of PLLA/hydroxyapatite composite. Polym Degrad Stab 149:152–161

Teitelbaum SL (2000) Bone resorption by osteoclasts. Science 289(5484):1504–1508

Wang C et al (2020) Synthesis and formation mechanism of bone mineral, whitlockite nanocrystals in tri-solvent system. J Colloid Interface Sci 569:1–11

Wang T et al (2021) Three-dimensional printing of calcium carbonate/hydroxyapatite scaffolds at low temperature for bone tissue engineering. 3D Print Addit Manuf 8(1):1–13

Wijnhoven IB et al (2020) Analysis of cell-biomaterial interaction through cellular bridge formation in the interface between hGMSCs and CaP bioceramics. Sci Rep 10(1):1–14

Wu Z et al (2020) Biomimetic and osteogenic 3D silk fibroin composite scaffolds with nano MgO and mineralized hydroxyapatite for bone regeneration. J Tissue Eng 11:2041731420967791

Yang W-F et al (2018) Surface-modified hydroxyapatite nanoparticle-reinforced polylactides for three-dimensional printed bone tissue engineering scaffolds. J Biomed Nanotechnol 14(2):294–303

Yang Y et al (2020) Magnesium-based whitlockite bone mineral promotes neural and osteogenic activities. ACS Biomater Sci Eng 6(10):5785–5796

Zhang J et al (2005) Crystal modifications and thermal behavior of poly (L-lactic acid) revealed by infrared spectroscopy. Macromolecules 38(19):8012–8021

Zhang H et al (2017) Crystallization behavior of poly (lactic acid) with a self-assembly aryl amide nucleating agent probed by real-time infrared spectroscopy and X-ray diffraction. Polym Test 64:12–19

Zhang D et al (2021) Core-shell poly (l-lactic acid)-hyaluronic acid nanofibers for cell culture and pelvic ligament tissue engineering. J Biomed Nanotechnol 17(3):399–406

Zhao L-S, Cai Y-H (2018) Studies of poly (L-lactic acid)/hydroxyapatite composites through DSC and XRD. In: IOP conference series: materials science and engineering, IOP Publishing

Zhou D et al (2017) Comparative study of porous hydroxyapatite/chitosan and whitlockite/chitosan scaffolds for bone regeneration in calvarial defects. Int J Nanomedicine 12:2673

Zhu Y et al (2019) Poly (l-lactic acid)(PLLA) coatings with controllable hierarchical porous structures on magnesium substrate: an evaluation of corrosion behavior and cytocompatibility. ACS Appl Bio Mater 2(9):3843–3853